

# **IMPROVING THE ACCURACY OF UAV IMAGE BLOCK ORIENTATION WITHOUT GCPS**

HONORE NIYONSENGA

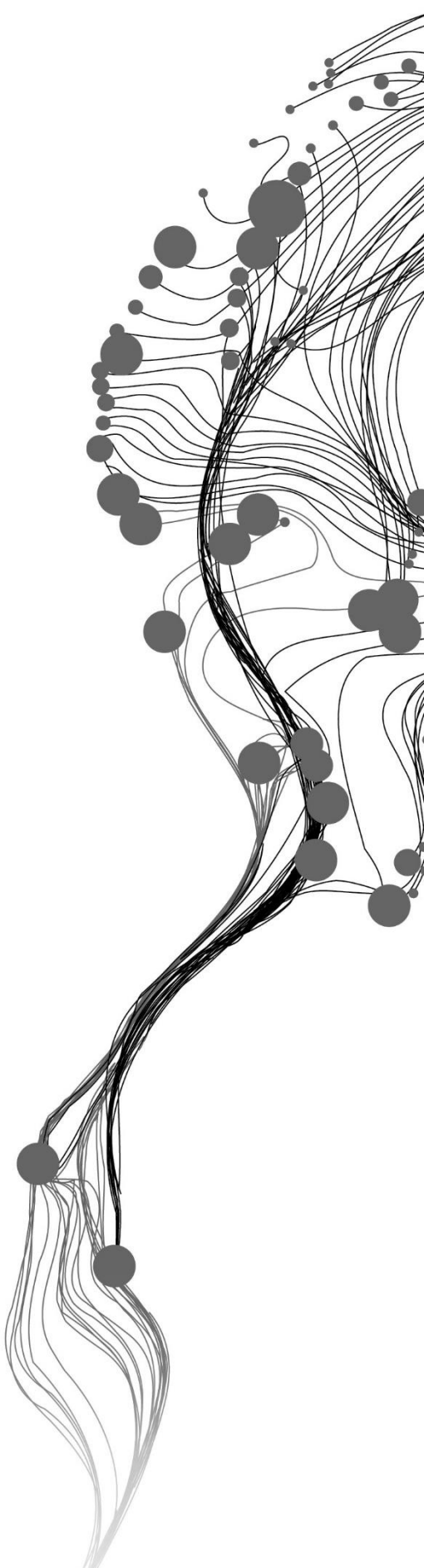
February, 2016

SUPERVISORS:

Dr. F. C. Nex

Dr. Ing. M.,Gerke





# IMPROVING THE ACCURACY OF UAV IMAGE BLOCK ORIENTATION WITHOUT GCPS

HONORE NIYONSENGA  
Enschede, The Netherlands,  
February, 2016

Thesis submitted to the Faculty of Geo-Information Science and Earth Observation of the University of Twente in partial fulfilment of the requirements for the degree of Master of Science in Geo-information Science and Earth Observation.  
Specialization: **Geoinformatics**

SUPERVISORS:  
Dr. F. C. Nex  
Dr. Ing. M.,Gerke

THESIS ASSESSMENT BOARD:  
Prof. Dr. Ir. M. G. Vosselman (Chair)  
Prof. Dr. Ing. Heinz-Jürgen Przybilla (External Examiner,  
Bochum University of Applied Sciences, Germany)

#### DISCLAIMER

This document describes work undertaken as part of a programme of study at the Faculty of Geo-Information Science and Earth Observation of the University of Twente. All views and opinions expressed therein remain the sole responsibility of the author and do not necessarily represent those of the Faculty.

## ABSTRACT

Nowadays drones were very used in civil applications and this technology has known a very fast spread in many sectors where it is adopted to compensate the limitations in traditional aerial photogrammetry. This is due to the high speed in rural-urban migration and economic development where there is an apparent growing need of more up-to-date, detailed and accurate maps for more diverse applications. Thereof, the UAV technology is used in many countries for various applications such as land administration, urban planning, agriculture and archaeology. The very fast popularity of this technology is attributable to its particular advantages like very high resolution, manoeuvrability, low cost and availability. However, the UAV photogrammetry has limitations related to low accuracy because of a consumer grade digital camera combined with low-cost GNSS/INS system on board in most of the cases.

As this accuracy can only be increased by an indirect orientation, more accurate ground truth information is required. In this regard, this project was conducted in order to find a solution to the low accuracy of UAV image block without using ordinary GCPs. And the main motivation is to maintain the low cost, flexibility and efficiency of this technology. Thereof, manual and automated methods were developed, implemented and tested using ISPRS Benchmark from Multiplatform Photogrammetry. In both methods, control points were detected, and measured from already available aerial orthophoto and elevation model in comparison to the UAV images block to be adjusted. As a result, a set of 3D control points were produced in aerial map coordinates system and used as ground truth to indirectly orient the UAV image block.

The experiments showed that the proposed two methods can reliably increase the accuracy in the image block oriented based only on geotags. In both manual and automated methods, the horizontal accuracy was increased from around 1 to 2 meters up to about 5cm, and the relative errors considerably corrected. From the current research and experiment, one can conclude that the proposed methods were effective and can be proposed in applications where such level of accuracy is sufficient.

**Keywords:** UAV image block orientation, Image block quality assessment, manual selection of GCPs, automatic selection of GCP, aerial orthophoto and DSM/DTM

## ACKNOWLEDGEMENTS

First and foremost, I praise Almighty God the Creator who guided me, protected and gave me good health and strength through my studies in Netherlands.

I would like to thank the Government of the Republic of Rwanda through Rwanda Natural Resources Authority (RNRA) for granting me a scholarship to study Geoformation Science and Earth Observation for geoinformatics at ITC-University of Twente.

I would like to express my sincere gratitude to my supervisors Dr F. C. Nex and Dr Ing M. Gerke for their irreplaceable support, commitment and constructive advises without which this research project would not be a success.

My sincere gratitude goes to my wife Marie Rose Nyirakamana and my daughter Audrey Gianna Niyonsenga for their love, patience, moral support and prayers during my studies away from home. The same gratitude goes to my family for always being supportive in my life and for their prayers.

I would like also to thank my friends in Europe for their moral support which have contributed a lot to the success of this research and feel again in the family while I was away from home.

Last but not least, my special thanks go to my classmates of GFM MSc. 2014-2016, for having selected me as their class representative, and their good collaboration, friendship and moral support. Furthermore, I owe gratitude to the ITC Students Association Board where I acted as Secretary General, and the entire ITC community for their moral support which has made my life at ITC become enjoyable.

## TABLE OF CONTENTS

---

<b>1. introduction</b>	1
1.1. Motivation and problem statement	1
1.2. Research identification	3
1.3. Innovation aimed at	3
1.4. Structure of the thesis	4
<b>2. LITERATURE REVIEW</b>	5
2.1. Introduction	5
2.2. Related work	5
2.3. UAV photogrammetry	6
2.4. UAV image block orientation	7
2.5. Summary	14
<b>3. PROPOSED METHODS</b>	15
3.1. Overview	15
3.2. UAV image-block quality assessment	16
3.3. Manual selection and measurement of control points	19
3.4. Automatic selection and measurement of control points	22
3.5. Summary	35
<b>4. RESULTS AND ANALYSIS</b>	37
4.1. Description of experimental data	37
4.2. Data quality analysis processes	37
4.3. Results of manually selected control points	41
4.4. Results of automatic selection of control points	43
4.5. Summary	47
<b>5. conclusions and recommEndations</b>	51
5.1. Conclusions	51
5.2. Answers to the research questions	52
5.3. Recommendations	53
List of references	55
appendices	59
Appendix 1: List of cameras	59
Appendix 2: List of control points	60
Appendix 3: List of control points and corresponding UAV image pixel coordinates	61
Appendix 4: Pix4d Mapper report on residual at CPs when manually selected control points were used	62
Appendix 5: Pix4d Mapper report on residuals at CPs when automatically selected control points were used along with DSM	63
Appendix 6: Pix4d Mapper report on residuals at CPs when automatically selected control points were used along with DTM	64

LIST OF FIGURES

---

**Figure 2-1:** Example of UAV platforms, **(a)** Aibot X6 Hexacopter Rotary Wing; **(b)** MAVinci SIRISIUS Pro Fix Wing..... 7

**Figure 2-2:** Pinhole camera model.  $C$  is a focal point (optical centre),  $c$  is a principal point,  $f$  principal distance,  $Z$  is optical axis;  $M$  is point on object;  $m$  is the point  $M$  in image  $I$ . On the Right hand, is the formula of the relationship between image coordinate and 3D space coordinate; Source: (Shapiro & Stockman, 2001) ..... 9

**Figure 2-3:** Epipolar geometry.  $C$  &  $C'$  are a focal points (optical centres) of two cameras,  $c$  is a principal point,  $Z$  is optical axis;  $M$  is a point on the object;  $m$  &  $m'$  are the point  $M$  in the images  $I$  &  $I'$  respectively. The line  $MM'$  is known as epipolar line, and plane  $\Pi$  is known as epipolar plane; Source: (Zhang, 1998)..... 9

**Figure 2-4:** Sequential registration of images in SFM , with the computation of Essential Matrices like  $E_{12}, E_{23}, E_{34}$ , that relate one view to its successor is performed successively from view 1 to view 7; Source: (Bolles & Baker, 1987) ..... 9

**Figure 2-5:** (a) Image scale(octave) and respective scale spaces(Gaussian images) produced from Gaussian analysis;(b) Difference-of-Gaussian images generated from adjacent Gaussian images. Finally, the Gaussian images are resampled down to factor two and the same process is repeated; Source: (Lowe, 2004) ..... 10

**Figure 2-6:** The detection of maxima and minima of Difference-of-Gaussian images were done by comparing one pixel(here marked by a black cross) to 26 neighbouring pixels in 3x3 regions in current and two adjacent images; Source: (Lowe, 2004) ..... 10

**Figure 2-7:** The illustration of the KP descriptors and corresponding image gradients where it is derived; Source: (Lowe, 2004) ..... 11

**Figure 2-8:** Rectangular area computation using an integral image; Source: (Bay et al., 2008) ..... 12

**Figure 2-9:** Example of detection of interest points; Source: (Bay et al., 2008) ..... 12

**Figure 2-10:** The interest point descriptor orientation assignment; Source: (Bay et al., 2008)..... 13

**Figure 2-11:** Inflight UAV image georeferencing; Source: (Benigno, 2012)..... 13

**Figure 3-1:** (a) Low accurate UAV image block with respect to the terrain; (b) Adjusted UAV image block and the terrain ..... 15

**Figure 3-2:** (a) Flowchart symbols; (b) Flowchart of processes for quality analysis of UAV image block .16

**Figure 3-3:** Example of the spatial plot of residuals at control points. Map elements: The purple bar for map scale of 10 cm on the ground; Yellow points for GCPs, Z-vectors in Blue and XY-vectors in Green. .... 18

**Figure 3-4:** Quality assessment of a horizontal linear structure in a DSM of Zollern dataset ..... 19

**Figure 3-5:** Overall workflow of processes of manual selection of control points from aerial imagery photogrammetric products ..... 20

**Figure 3-6:** Control points selection from aerial orthophoto on left side and UAV orthophoto on right side. .... 21

**Figure 3-7:** Flowchart of processes for automatically select control points from aerial imagery products 23

**Figure 3-8:** Limitation of the AOI for KPs detection and descriptor matching for one UAV image and aerial orthophoto ..... 25

**Figure 3-9:** Example cases of SURF KPs detection and descriptors computation in UAV image (on left) and aerial orthophoto mask (on right). Green circles are KPs descriptors' illustrations showing the size and orientation of the change gradient of the pixels grey values in the detected KPs' neighbourhood..... 25

<b>Figure 3-10:</b> SURF KPs descriptors matching without any filtration. The green lines connects two corresponding points in both UAV (on left) and aerial image (on right).....	26
<b>Figure 3-11:</b> Aerial photography where homography takes a map as perspective view of the ground; Source: (CorrMap, 2015) .....	27
<b>Figure 3-12:</b> Raw KPs pairs' matches between a UAV image P1000529_1400494888594.JPG (on left) and aerial orthophoto mask (on tight) with 73 matches; Examples of results of RANSAC matches filtration with different thresholds: 20, 19, and 13 inliers out of 73 matches for 20.0, 10.0 and 5.0 threshold values respectively.....	28
<b>Figure 3-13:</b> Aerial orthophoto ground surface classification for control points search area demarcation. Light yellow is demarcated search area; dark yellow rectangle is the boundary of the entire study area .....	29
<b>Figure 3-14:</b> (a)List of images and corresponding camera positions; (b)List of selected and filtered unique control points; (c) List of control points and corresponding UAV image marks (pixel locations).....	30
<b>Figure 3-15:</b> List of UAV camera data preparation in case a DSM is used as elevation model. ....	33
<b>Figure 3-16:</b> Demarcation for search area in case a DTM is used as elevation model. Yellow rectangular is the entire study area, and the light yellow coloured areas are the masked ground surfaces .....	34
<b>Figure 4-1:</b> The project study area, at Zeche Zollern in Dortmund –Germany; Source: (Google Earth Pro, 2016) .....	37
<b>Figure 4-2:</b> Absolute residuals at CPs (a) when only geotags are used and (b) When ordinary accurate GCPs were used.....	38
<b>Figure 4-3:</b> Spatial plot of residuals at CPs in $X, Y, Z$ components in UAV image block (a) when only geotags were used and (b) when ordinary accurate GCPs were used. Purple bar is scale bar of 10 cm on ground, Green vectors are XY-residuals, and Blue vectors are for Z-residuals.....	38
<b>Figure 4-4:</b> UAV image relative accuracy assessment on the points on one horizontal line of features in the Zollern dataset.....	39
<b>Figure 4-5:</b> Residuals at CPs in $X, Y, Z$ components in 3 different distributions of GCPs around the scene. Yellow points are GCPs and purple bar is scale bar of 40 cm on ground., Green vectors are XY-residuals, and Blue vectors are for Z-residuals .....	40
<b>Figure 4-6:</b> Absolute residuals at CPs when manually selected control points are used .....	42
<b>Figure 4-7:</b> Spatial plot of residuals at CPs in UAV image block when manually measured control points are used. Purple bar is a scale of 10 cm on the ground, Green vectors are XY-residuals, and Blue vectors are for Z-residuals.....	42
<b>Figure 4-8:</b> Absolute residuals at checkpoints when automatically selected control points and DSM were used .....	44
<b>Figure 4-9:</b> Spatial plot of residuals at CPs in UAV image block when automatically measured control points and DSM are used. The scale is bar is a unit of 10 cm on the ground, GCPs are yellow points, blue vectors and green are Z-vector and XY-vectors respectively.....	45
<b>Figure 4-10:</b> Example of results of control points selection when a DTM is used as elevation model. (a) The light green shows the masked area for control points located on the open ground surface. Dark brown points a selected control points resulted from the automated method. (b) & (c) Show in large two examples of selected points on the aerial orthophoto (Right side) and some corresponding UAV images where it is visible(Left side). The orange circle mark the selected control point. ....	46
<b>Figure 4-11:</b> Absolute residuals at checkpoints when automatically selected control points located on ground surface were used.....	47
<b>Figure 4-12:</b> Spatial plot of residuals at CPs in UAV image block when automatically measured control points located on the ground surface only are used. The scale is bar is a unit of 10 cm on the ground, GCPs are yellow points, blue vectors and green are Z-vectors and XY-vectors respectively .....	47

**Figure 4-13:** RMSE of residuals at CPs in *X, Y, Z* components, when different types of control points were used for indirect orientation of the UAV image block.....48

**Figure 4-14:** RMSE of residuals at CPs *X, Y, Z* components with RTK-GNSS enabled; on left cross-flight patterns are used, on right no cross-pattern used in 3 different configurations of GCPs; Source: (Gerke & Przybilla, 2016).....49

**Figure 4-15:** RMSE of residuals at CPs *X, Y, Z* components without RTK-GNSS and based on control points (From left to right) Manually selected with DSM, automatically selected with DSM, automatically elected with DTM .....49

LIST OF TABLES

---

**Table 3.1:** The UAV image corresponding extent estimation from aerial orthophoto. With minimum and maximum values in  $x$  and  $y$  being  $Minx, Miny, Maxx, Maxy$ ; and buffer size in meters:  $n$  ..... 24

**Table 4.1:** Average estimation of deformation quantification of the UAV image block in Zollern dataset after the orientation using geotags only ..... 40

**Table 4.2:** Average relative error quantification of the UAV image block in Zollern dataset after the orientation using control points manually measured from an aerial orthophoto and DSM ..... 43

## LIST OF ABBREVIATIONS

---

2D	Two Dimension
3D	Three Dimension
AOI	Area Of Interest
CP	Check Point
DSM	Digital Surface Model
DTM	Digital Terrain Model
GCP	Ground Control Point
GNSS	Geographic Navigation Satellite System
GSD	Ground Sampling Distance
GPS	Geographic Position System
KP	Key Point
INS	Inertial Navigation System
ISPRS	International Society for Photogrammetry and Remote Sensing
RANSAC	Random Sampling Consensus
SIFT	Scale Invariant Feature Transform
SURF	Speeded-Up Robust Features
RTK	Real Time Kinematic
UAV	Unmanned Aerial Vehicle

## 1. INTRODUCTION

### 1.1. Motivation and problem statement

In recent years, aerial photography has been quickly adopted in many countries for land surveying and cadastral boundary mapping due to its efficiency as compared to traditional methods. However, because of the high speed in social and economic development, there is an apparent growing need of more up-to-date, detailed and accurate maps for more diverse applications. In this regard, the Unmanned Aerial Vehicle (UAV)-based photogrammetry has been developed to compensate the limitations in conventional aerial photogrammetry. This light aircraft operates without a physical human operator on board. In the geomatics domain, it is mainly used for Digital Surface model or Digital Terrain model (DSM or DTM) generation, image processing for Two-Dimension (2D) or Three-Dimension (3D) feature extraction, orthophoto generation and 3D modelling. However, the quality of these products depends on some important factors such as camera resolution, flight height and accuracy in Ground Control Points-GCPs (Berteška & Ruzgienė, 2013; Ahokas, Kuittinen, & Jaakkola, 2000). Generally, the needed accuracy and spatial resolution depend on the specific purpose of the actual mapping.

Hence, in case a land mapping is based on aerial photogrammetry, the positional accuracy required in the final products should be taken into consideration. For example, in Fgdc (1998), the Federal Geographic Data Committee (FGDC) Geodetic sub-committee describes the way the accuracy can be reported based on relative error cycle at 95% confidence interval. This georeferencing relative accuracy also referred to as local accuracy, is suitable for cadastral boundary surveys because it represents the uncertainty of the coordinates of a point relatively to the another one to which it is directly connected. In other words, it measures how points are positioned relatively to each other. On the other hand, the absolute error is the measurement of how far off is the point in respect to the true value which is ground control point information in the mapping frame. Consequently, georeferencing in aerial photogrammetry must be taken care of as a good precision is needed. And this can be achieved by direct georeferencing during the flight and photography process based on sensor systems on board, or indirectly in post process using external ground truth information as control points.

The conventional aerial imagery is based on manned aircraft equipped with high-end photogrammetric mid or large frame cameras, and differential Geographic Position System –Inertial Measurement Unit (GPS-IMU) systems for highly accurate direct sensor orientation and positioning. However, this approach has a number of limitations that have been a topic of many types of research in recent years. These disadvantages are, for example, high cost, restricted manoeuvrability, occlusions by the clouds and limited availability. However, modern and high-end imaging systems like Visionmap (2015) used in these large airborne platforms can reach a Ground Sampling Distance (GSD) of 5 centimetres with a very high positional accuracy which satisfies the requirements in most of the applications. Nevertheless, in some places, mostly in developing countries, the maps currently in use for cadastre and land administration were produced using sophisticated and quite expensive aerial photogrammetric systems. Therefore, in many cases, it is quite challenging to use the same aerial imagery technology to update those maps although it is highly necessary. This is because of the relatively high cost of these advanced systems. Fortunately, there is an opportunity of using a more flexible and low-cost UAV

imagery that can take care of the limitations in the traditional method as well as the high need for constant up-to-date maps for many applications.

Used in Land surveying and mapping, these light-weight autonomous platforms have a Global Navigation Satellite System (GNSS) receivers on board, to provide information on the position and altitude, vertical and horizontal projection level, and the time at which the images were taken (TERRISGPS, 2015). Nowadays, there is a variety of UAV systems available on the market for aerial photogrammetry. However, because of limited payload in this lightweight aircraft, it is not possible to transport a GPS/INS system on board for accurate direct sensor orientation and corrections of errors related to the sensor attitudes (pitch, yaw, and roll). Consequently, in most of the cases the UAV platforms use consumer grade sensors which do not have enough accuracy. However, nowadays the use of Real Time Kinematic(RTK)-GPS system in UAV imagery, like EBee (2015) and MAVinci (2015), in combination with a reference station and, at least, one ground station, can reach 2-5cm accuracy. But still, this system is relatively expensive. Therefore, low cost, simple system and autonomous platform with a consumer grade GNSS are used in most of the cases (Nex & Remondino, 2013). As a consequence, accurate ground control information and image block post-processing are required to reduce block deformation and correct absolute position offset in the UAV imagery products.

For the above-mentioned reasons, the GCPs are very important and essential for a better accuracy in the UAV image bundle adjustment (Nex & Remondino, 2013; Schenk, 2005). Moreover, the number of GCPs to be used and their distribution around the scene depends on the size and topography of the terrain. Thus, the selection and measurement of these control points need some level of expertise in land surveying. However, the use of control points measured on the field using traditional methods has also some limitations. These disadvantages are, for example, the acquisition cost, intensive labour, cumbersome manipulations. In some cases, it is not possible to take proper measurements because of multipath effects and GPS occlusion, and some areas are not even accessible. Therefore, there is a need to find out if there is a possibility to orient the UAV image block based on a source of information other than the ordinary GCPs. In this regard, the opportunity to use the information from traditional aerial photogrammetry for UAV image block adjustment is the main goal of this proposed research project. In this way, aerial imagery photogrammetric products being already available with good accuracy can be used to improve the georeferencing of more recent and low-cost UAV images of the same area that were acquired using lower accurate GNSS and navigation systems.

## 1.2. Research identification

### 1.2.1. Research objectives

The primary objective of this research is to develop a reliable, efficient and flexible approach to increase the accuracy of the absolute orientation of UAV image block as well as reducing the eventual deformations without using ordinary GCPs, but based only on the information extracted from already existing aerial orthophoto and elevation model.

The following sub-objectives have to be accomplished in order to achieve the mentioned main objective:

- To assess the quality of the direct georeferenced (geotag) UAV image block using accurate and well-distributed GCPs.
- To process the UAV image block in order to improve geolocation accuracy and correct eventual deformations, based only on the information manually measured from existing aerial orthophoto and elevation model.
- To develop and implement an automated method for improving the accuracy of the UAV image block using only as reference the information generated from the aerial orthophoto and elevation model.

### 1.2.2. Research questions

In order to achieve the main objective of the current research, the following research questions need to be answered:

- What is the geo-location accuracy of the UAV image block direct georeferencing?
- How much deformation is in the available direct georeferenced UAV image block?
- How to manually find and extract homologous points from existing lower resolution aerial orthophotos and UAV images?
- How to get height values from available elevation model to 2D points selected as control points in both UAV images and aerial orthophoto?
- How reliable and accurate is the use of the manually selected control points to perform the UAV image block adjustment?
- How to automatically find and extract homologous points in both UAV image and aerial imagery photogrammetric products?
- How can accurate UAV image block adjustment be achieved based on automatically detected and extracted control points from already available aerial imagery products?

## 1.3. Innovation aimed at

To propose reliable and efficient approaches that base on ground truth control points other than ordinary GCPs to adjust a UAV image block that is initially oriented using approximate geotags information. Thereof a manual and automated methods were proposed for the acquisition of ground truth information based only on already available lower resolution but more correctly georeferenced aerial orthophoto and elevation model.

#### 1.4. Structure of the thesis

This thesis is written as a report of the project done in order to find a solution to the above-mentioned research questions. It is composed of five chapters:

##### **Chapter 1: Introduction**

In this chapter, a general overview of the project is presented in the form of motivation, problem statement, research identification and innovation aimed at.

##### **Chapter2: Literature review**

This chapter presents some literature of this projects related works. This is done by providing a general overview of the field of research, what other people did before and the main technology used in this project.

##### **Chapter3: Proposed method**

In this chapter, proposed methods and their implementations are described. Thereof, a method of UAV image block quality analysis is proposed, as well as two methods of increasing the accuracy of that dataset without using ordinary GCPs, but only based on aerial imagery photogrammetric products.

##### **Chapter4: Results and analysis**

In this chapter, the experiment data is described and different results of the implementation of the proposed methods were presented.

##### **Chapter5: Conclusions and recommendation**

In this chapter, a general conclusion is drawn, answers to the research questions presented, and finally an overall recommendation is given.

## 2. LITERATURE REVIEW

### 2.1. Introduction

In this chapter, an outline of the literature review is presented in order to provide a clear understanding of the current research field. This is done by indicating some related projects conducted in the UAV image orientation domain and an overview of the core technology used in the automation of the process. First the example of related work is presented; then an overview of the technology used in UAV for land surveying photogrammetry is also summarized, and finally SIFT and SURF computer vision algorithms are also presented.

### 2.2. Related work

In recent years, the UAV technology has been an interesting field of research in the remote sensing and photogrammetry. These light-weight aircraft are designed in different airframes but the main ones are fixed and rotary wings presented on Figure 2-1 (Nex & Remondino, 2013). In addition to that, due to the low payload capacity in these light-weight aircraft, they can only carry on board a simple and light consumer grade digital camera combined with low-cost GNSS/INS system. Thus, the photogrammetric products generated from that technology are of a relatively low accuracy. Therefore, this issue has interested many researchers and a good number of projects were conducted in order to find a solution to the UAV image block deformation and quality of georeferencing process. Generally, these types of research can be categorized into three main groups.

First, there are researches conducted and proposed automated techniques for UAV image block orientation based on Point clouds generated from different sources such as (i) Structure From Motion (SFM) by Turner, Lucieer and Watson(2012), Barazzetti, Remondino, and Scaioni (2010), Luigi Barazzetti, Forlani, Remondino, Roncella, & Scaioni (2011) and (ii)Laser scanning by Wallace, Lucieer, Watson and Turner(2012), and Xu et al.(2014).

Second, the image block orientation using other images as reference, where (i) Gerke (2011) and(ii) Gerke and Nyaruhuma (2009) proposed the use of buildings' vertical and horizontal information for bundle adjustment; (iii) Oh, Toth, and Grejner-brzezinska (2010) proposed an automated approach of indirect georeferencing an aerial image block on high accurate satellite imagery products; (iv) Han, Byun, Choi, Han and Kim (2012) proposed an automated method of co-registering mini-UAV images within a single frame, by first detecting the control points, then perform image transformation, and finally do the image resampling; (v)Wang, Stefanidis, Croitoru, & Agouris (2008) proposed an automated method of registering UAV image sequences based on existing map linear features.

Thirdly, several studies were also conducted in the quality assessment of the UAV imagery products in various application fields such as Küng et al. (2012); Harwin and Lucieer (2012); Eisenbeiss and Zhang (2006); Chiabrando, Nex, Piatti and Rinaudo (2011) and Zarco-Tejada, Diaz-Varela, Angileri and Loudjani (2014).

In all these past research projects, one can easily see that there is an apparent interest in using the UAV imagery products in various applications that have inspired many researchers in this field. And in order to achieve that, a post-process is needed for the whole bundle block adjustment using the ground control points or any other reference. In order to use UAV in any aerial photography for any application, one must have an overview of the pipeline of processes and related technologies used in the image acquisition and post-processing. So, in the following sections, the UAV photogrammetry's main processes are going to be briefly described, as well as related image analysis and processing technologies

### 2.3. UAV photogrammetry

Unmanned Aerial Vehicle –UAV is a common name attributed to all autonomous or remotely controlled aircraft. This expression is mostly used in computer science, but other terms are also used, such as drones, robot plane, pilotless aircraft, Remotely Piloted Vehicle(RPV), Remotely Operated Aircraft (ROA), Remote Controlled Helicopter (RC-Helicopter), Unmanned Vehicle System (UVS) and Model Helicopters (Eisenbeiss, 2004; Bone & Bolkcom, 2003; Remondino, Barazzetti, Nex, Scaioni, & Sarazzi, 2011). In past, this technology was developed and applied mainly for military goals (Bone & Bolkcom, 2003). But in recent years, the UAVs have been used in civil applications such as land administration, Urban planning, Agriculture, Archaeology. And many types of research are currently being conducted in this field. This is justified by a high speed in development of new and low-cost platforms combined with consumer grade digital cameras and GNSS. However, despite its rapid spread in number and variety, the UAV use is still limited by airspace regulations which are still not yet ready in many of countries. Moreover, nowadays this technology has promoted the use of remote sensing for sufficiently acquiring data at very low cost (J. Everaerts, 2008). This is due to the fact that UAV is able to conduct a photogrammetric data acquisition using the relatively cheap consumer grade digital camera in combination with low-cost GPS-INS system and is easy to manipulate.

Basically, a proper workflow of processes for data acquisition using UAV involves a flight plan, GCPs measurements, image acquisition and image orientation (Remondino et al., 2011). (i) The flight plan is performed on a personal computer using a dedicated software. In this stage, the following parameters are determined: AOI, GSD, onboard camera internal parameters, forward-lap and side-lap percentage (Eisenbeiss, 2004). (ii) It is also a good practice to measure the GCPs and mark them before the flight so that it may be easy to recognize them in the images while indirectly orienting the image block from the laboratory or office. In addition to that, the GCPs have to be well selected and measured using high accurate geodetic systems. (iii) The taking off and landing of the aircraft depends on the properties of the platform, but in most of the cases, these operations are monitored and remotely controlled by a pilot. Then, the images are taken according to a planned intervals (iv). The acquired images are processed and produce dense DSM, 3D models, high-resolution orthophotos and other related photogrammetric products (Haarbrink & Eisenbeiss, 2008).

When a proper photogrammetric process pipeline is applied, the above-mentioned products can be produced in the very efficient way (Grenzdörffer, Engel, & Teichert, 2008). This is possible by recently developed automated methods of surface reconstruction and feature extraction based on known camera parameters (Remondino et al., 2011). As results, nowadays a variety of the automated production of a dense DSM and above mentioned derived products using commercial or open sources software applications are available. For example, Pix4d Mapper, APERO, MICMAC, Microsoft Photosynth, Bundler, CMVS/PMVS2 and AgiSoft Phoscan as listed by Neitzel & Klonowski (2012) and Pierrot Deseilligny & Clery (2012). Therefore, this technology development that continues to spread all over the world has made the use of UAV a popular photogrammetric data acquisition for various applications. However, this method can only be accepted when it has a required accuracy and is competitive in terms of cost as compared to the other technologies (Sauerbier, Siegrist, Eisenbeiss, & Demir, 2012). These applications are diverse, and some of them are for example videography/Photography, Marketing, Real Estate, Urban planning, Education, Environnement and climate management, Insurance, Aviation, Meteorology, Tourism, Utilities, Mining, Mapping, Construction/Pre-construction, Maritime and Agriculture (AIR-VID, 2015)



**Figure 2-1:** Example of UAV platforms, (a) Aibot X6 Hexacopter Rotary Wing; (b) MAVinci SIRISIUS Pro Fix Wing

#### 2.4. UAV image block orientation

UAV is used in surveying mainly for the production of DSM or DTM, 3D model, feature extraction and orthophoto after initial camera calibration and image triangulation (Nex & Remondino, 2013).

- **The image calibration** is a photogrammetric process whereby intrinsic and extrinsic camera parameters are estimated (F. Ke, Xie, & Chen, 2016). As it is clearly illustrated in Figure 2-3, the intrinsic parameters are principal point  $c$  and principle distance  $f$  and external parameters are  $X, Y, Z$  world coordinates of the projection centre  $C$ , plus its rotation and translation parameters.
- **The image triangulation** is defined as the process of estimation of 3D point position based on multiple 2D images points where it is seen (Gries & Schneider, 2010). This scenario is well illustrated in Figure 2-3, where a 3D coordinates of the point  $M$  is estimated based on 2D coordinates of two points  $m$  and  $m'$  of the image  $I$  and  $I'$  respectively where it is visible.

During image acquisition, the aircraft flies and takes photos according to a planned schedule and communicating with a ground pilot's platform. This autonomous aircraft has a GNSS/INS devices to guide and record the position of the camera during the flight. However, due to the low payload, the sensors used are very light, thus with low quality in terms of accuracy as compared to the ones used in bigger platforms like aircraft and satellites. Consequently, images registration and georeferencing is indispensable for more reliable results.

##### 2.4.1. UAV image registration

Based on metadata (geotags and times of acquisition) the UAV images are processed in sequence by relatively correcting camera position and orientation information of a camera relatively one by one (Yahyanejad, Wischounig-Strucl, Quaritsch, & Rinner, 2010). This process is performed on the image to image registration basis using SFM computer vision technology. In this case, SFM allows to relatively orient overlapping images, thereafter, an absolute orientation can be performed using both GCPs and/or GNSS information also known as geotags. SFM is described and explained in details, in the following section.

Thereof, SFM uses an automatic extraction of homologous point features in two or more images to develop 3D models from a sequence of overlapping images (Turner et al., 2012). That is the reason why in recent years scientists in the computer vision community have developed a variety of image matching algorithms. For example VLFeat (Vedaldi & Fulkerson, 2010), Oriented Fast & Rotated BREF (ORB) (Rublee, Rabaud, Konolige, & Bradski, 2011), Principal Component Analysis (PCA) (Y. Ke & Sukthankar, 2004), Binary Robust Invariant Scalable KPs (BRISK) (Leutenegger, Chli, & Siegwart, 2011) and Speed Up Robust Features (SURF) (Bay, Ess, Tuytelaars, & Van Gool, 2008), have contributed a lot in the automation of the

camera calibration and image orientation. Most of these algorithms are newer as compared to the famous Scale Invariant Feature Transform (SIFT) (Lowe, 2004) and Speeded Up Robust Feature (SURF) technologies. So, SFM has become very popular in UAV automatic image registration solutions.

#### **2.4.1.1. Structure From Motion (SFM)**

SFM is one of the most used technics in computer vision for real scene image-based 3D modelling due its simple and easy usability (Wei, Kang, Yang, & Wu, 2013). This technic workflow is mainly composed of three steps. (i) Tie points collection, (ii) Estimation of camera positions and orientation in 3D, (iii) and bundle block adjustment. In the following sections, the above-mentioned elements are briefly explained.

##### **Tie points collection**

The tie points are collected in overlapping images by detecting and extracting corresponding point pairs from images sequences. In this case, SIFT is the most used due its strong capability of detecting invariant points from images of different scales, rotations and illumination (Turner et al., 2012). For more details, SIFT technology is detailed bellow in section 2.4.4.

##### **Estimation of camera position and pose**

The estimation of the camera position and orientation is performed based on epipolar geometry and image triangulation concepts.

By epipolar geometry, two perspective images of the same objects are assumed to be related by a 3x3 matrix by which 3D points are projected into 2D image points (Zhang, 1998). This matrix known as Fundamental matrix and estimated based on Pinhole Camera model as demonstrated billow on Figure 2-2 bellow. And the Epipolar geometry is illustrated in Figure 2.3

##### **Multiple-view Structure From Motion**

As for two overlapping images, a fundamental matrix is determined as a presentation of the geometric relationship between two pairs of views, in this section, a further attention is taken at solving a problem of in case of a given number of views. In this case, a sequence of image views is processed by first finding two views for initial 3D reconstruction, and for every additional view, integrate successive view one by one and continuously refining camera pose of the new with regard to the previous one based on images matching features (Bolles & Baker, 1987). The scenario is illustrated in Figure 2-4 where initial Essential Matrix  $E_{12}$  is computed between two initial vew1 and view2, and Essential Matrix  $E_{23}$  computed between view2 and view3, and so on throughout the entire sequence of views. The final step after this, is the bundle block adjustment which usually requires external control points for the correction of the entire geometry of the image block.

##### **Bundle block adjustment**

Images bundle adjustment is a technique used to correct overall re-projection errors by refining the estimate of 3D scene reconstruction (Liu, Yu, Maier, & Manner, 2003; Bolles & Baker, 1987). The main objective being to fit the reconstructed model to the terrain based on the ground truth information. These GCPs provide a terrain coordinate system into which the entire model is transformed.

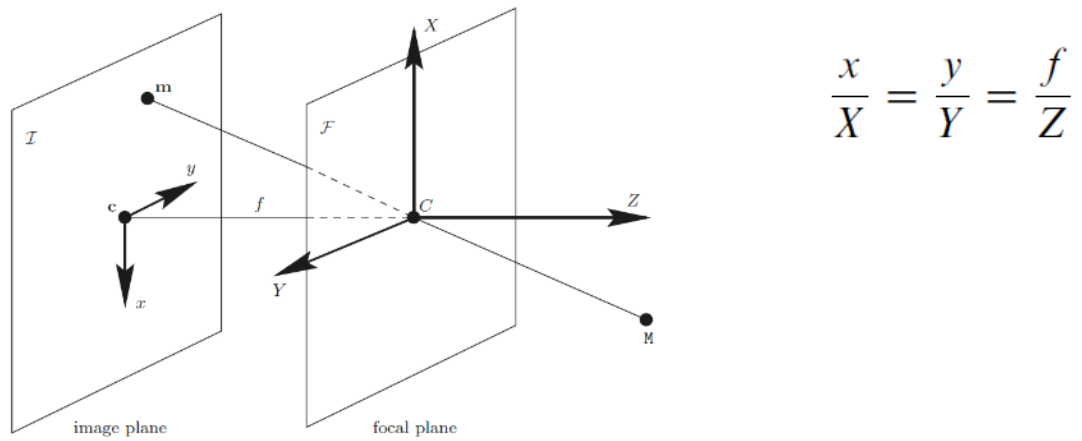


**Figure 2-2:** Pinhole camera model.  $C$  is a focal point (optical centre),  $c$  is a principal point,  $f$  principal distance,  $Z$  is optical axis;  $M$  is point on object;  $m$  is the point  $M$  in image  $I$ . On the Right hand, is the formula of the relationship between image coordinate and 3D space coordinate; Source: (Shapiro & Stockman, 2001)

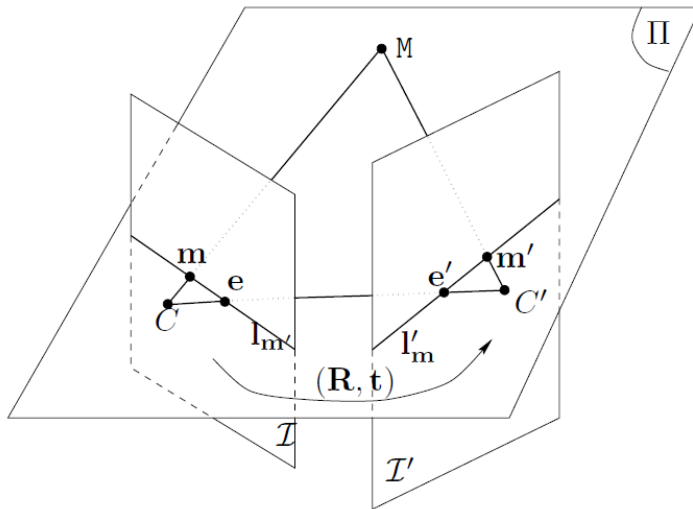


**Figure 2-3:** Epipolar geometry.  $C$  &  $C'$  are a focal points (optical centres) of two cameras,  $c$  is a principal point,  $Z$  is optical axis;  $M$  is a point on the object;  $m$  &  $m'$  are the point  $M$  in the images  $I$  &  $I'$  respectively. The line  $mm'$  is known as epipolar line, and plane  $\Pi$  is known as epipolar plane; Source: (Zhang, 1998).

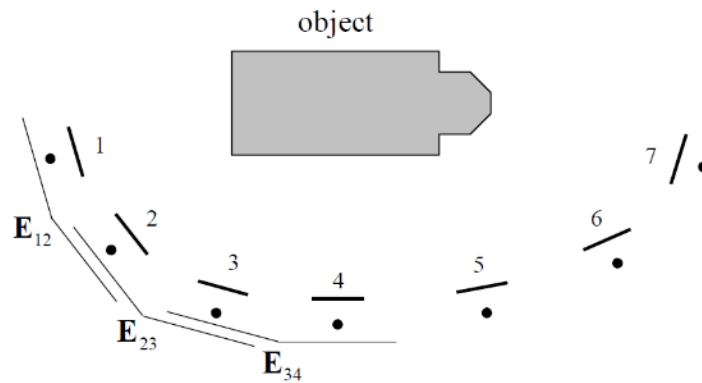


**Figure 2-4:** Sequential registration of images in SFM, with the computation of Essential Matrices like  $E_{12}$ ,  $E_{23}$ ,  $E_{34}$ , that relate one view to its successor is performed successively from view 1 to view 7; Source: (Bolles & Baker, 1987)

### 2.4.1.2. Scale Invariant Feature Transform (SIFT)

This computer vision technology was developed by David G. Lowe of University of Columbia and is used to extract distinctive invariant features from images used as tie points in matching different images from different perspective views (Lowe, 2004). Thereof, the approach used in the recognition of the Keypoints (KP) is summarized in four main steps: (i) Scale-space extrema detection, (ii) KPs localization (iii) Orientation assignment and (iv) KP descriptor computation.

- **Scale-space extrema detection**

On this step, the algorithm searches in all the scales and all around the image extent and detect the candidate scale and orientation invariant points. This is done by resampling the image into a defined number of levels know as Octaves, and producing a Difference-of-Gaussian image from adjacent images as illustrated in Figure 2-5 below.

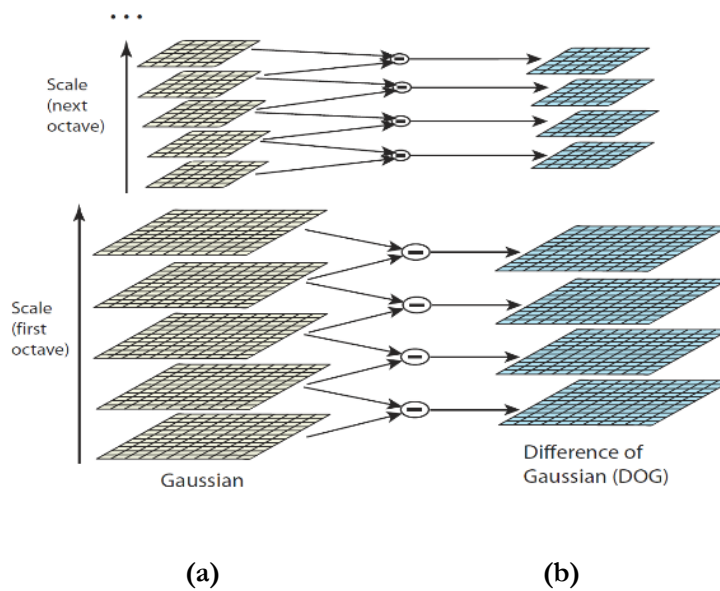


**Figure 2-5:** (a) Image scale(octave) and respective scale spaces(Gaussian images) produced from Gaussian analysis;(b) Difference-of-Gaussian images generated from adjacent Gaussian images. Finally, the Gaussian images are resampled down to factor two and the same process is repeated; Source: (Lowe, 2004)

Then, the KPs locations are detected using scale spaces extrema and minima in the Difference-of-Gaussian images as illustrated in Figure 2-6 below. This is done by comparing each pixel to its neighbouring 8 pixels on the same image plus 9 on the image above and 9 on the image below.

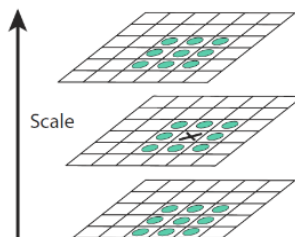


**Figure 2-6:** The detection of maxima and minima of Difference-of-Gaussian images were done by comparing one pixel (here marked by a black cross) to 26 neighbouring pixels in 3x3 regions in current and two adjacent images; Source: (Lowe, 2004)

- **KPs localization**

After the above step, each KP candidate is examined for stability based on its location and scale. The minima and maxima define the orientation, the scale and location of the KPs. Thereafter, a minimum contrast threshold is applied and the low contrast KPs candidates are rejected. Finally, the Difference-Of-Gaussian helps also at determining the point along the edges, which have to be eliminated also and remain with only with strong, invariant and distinct KP.

- **Orientation assignment**

To each KP image location, one or more directions are set based on a measure of the gradients. These orientations define the properties of the descriptors that allows them to keep the information on rotation invariance

- **KP descriptor computation.**

After the computation of the gradients in the KP region, they all are accumulated into a summarized histograms of their properties in 4x4 sub-regions around the concerned points. This process is clearly illustrated in Figure 2-7 below.

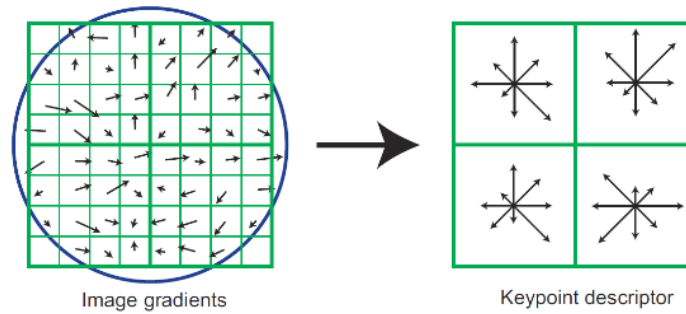


**Figure 2-7:** The illustration of the KP descriptors and corresponding image gradients where it is derived; Source: (Lowe, 2004)

For a more detailed description of the algorithm, please refer to Lowe (2004).

### 2.4.1.3. Speeded Up Robust Features (SURF)

SURF algorithm was developed after SIFT, and the main objective was to speed up the KP detection and descriptors computation and maintain the performance (Bay et al., 2008). This was achieved by simplifying the KP detection process and reducing the size of the descriptors. Thereof, the following steps are performed in the SURF process workflow.

#### Integral image

In order to detect the interest points, this algorithm uses by a basic Hessian Matrix approximation to the integral images. These images are computed based on box-type convolution filters. Whereby, the value of an integral image at pixel location  $(x, y)$  is computed as a summation of all pixel values in  $x$  and  $y$  of an input image within a rectangular area defined around that point.

Given, input image  $I$ , Point  $(x, y)$ , the integral image is calculated as the following formula

$$I_{\Sigma(x,y)} = \sum_{i \leq x} \sum_{j \leq y} I(x, y)$$

**Equation 2.1:** Computation of an integral

After the computation of the integral image, the sum of intensity of a rectangular area of an image (A, B, C, D) is calculated by A-B-C+D as illustrated on the image below in Figure 2-8:

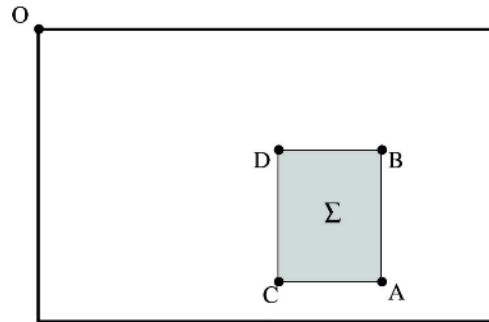


**Figure 2-8:** Rectangular area computation using an integral image; Source: (Bay et al., 2008)

### Hessian matrix based interest point

Using the Hessian matrix, the image is filtered in order to find the maxima and minima in different regions based on the values of the determinants. This is done using the following kernel in Equation 2.2:

$$\mathcal{H}(\mathbf{x}, \sigma) = \begin{bmatrix} L_{xx}(\mathbf{x}, \sigma) & L_{xy}(\mathbf{x}, \sigma) \\ L_{xy}(\mathbf{x}, \sigma) & L_{yy}(\mathbf{x}, \sigma) \end{bmatrix}$$

**Equation 2.2:** The computation of Hessian matrix in  $\mathbf{X}$  at scale  $\sigma$ . The matrix members are the second derivative of the Gaussian of the image

### Scale analysis with constant image size

SURF uses different image scales to find the right interest points as it is in SIFT. But SURF applies the up-scaled Box filters on the integral image instead of using the same filter for iteratively reducing the images. This component gives this algorithm a computation efficiency property.

### Localization of interest point

For the detection of the interest point, the algorithm proceeds by the exclusion of non-maxima in the 3x3x3 neighbourhood in the image and all the scales. An example where KPs were detected and descriptors computed is illustrated in Figure 2-9 below.

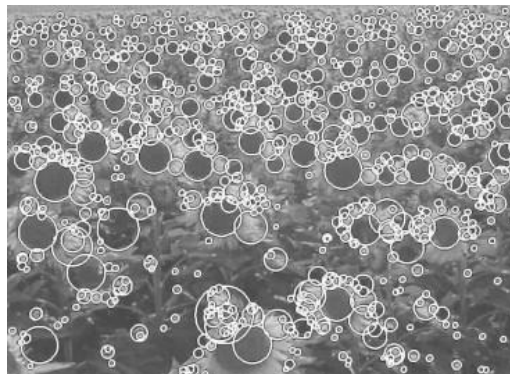


**Figure 2-9:** Example of detection of interest points; Source: (Bay et al., 2008)

The KP descriptors are computed in the neighbourhood of the interest points the same in SIFT, and the orientation is also determined in order to maintain its reproducibility. The Figure 2-10 illustrate how an orientation is assigned to a KP descriptor.

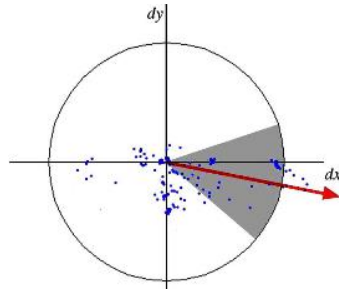


**Figure 2-10:** The interest point descriptor orientation assignment; Source: (Bay et al., 2008)

#### 2.4.2. UAV image georeferencing

From above sections, overlapping images were relatively oriented based on homologous features marching in initial positions of the cameras which may be known or completely unknown. Thus, there is a need for the determination of absolute positions of the cameras in the ground coordinate system. This process is referred to as georeferencing. Basically, there exist two main ways of doing that. The first one is the direct georeferencing where a camera is assigned a position and orientation during image acquisition using the GNSS-INS system on board. The second one is indirect georeferencing where measurements taken on the ground were introduced in the imagery post processing for absolute orientation.

##### 2.4.2.1. UAV image direct georeferencing

A direct georeferencing process is an immediate assignment of geographic position and orientation information of the sensor to the remotely acquired data of the ground without using ground-based measurement (Hemerly, 2014; Mostafa, Hutton, & Lithopoulos, 2001). In the case of UAV-based photogrammetry, this light aircraft uses its integrated sensor system to assign geographic tags (geotags) on each image based on time stamps information saved in the flight mission image data combined with and GPS data ( MarcusUAV inc, 2014). For more explanation, this scenario is illustrated in Figure 2-11. As a result, the geotags are very useful in image orientation and 3D modelling.

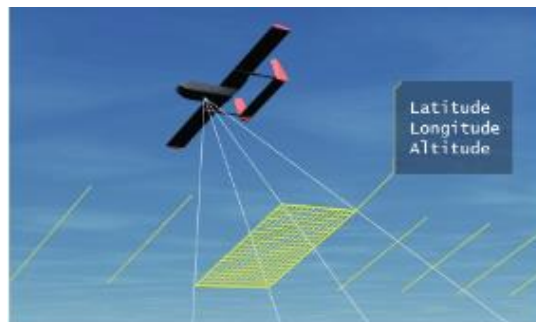


**Figure 2-11:** Inflight UAV image georeferencing; Source: (Benigno, 2012)

#### **2.4.2.2. UAV image indirect georeferencing**

In UAV photogrammetry, an initial image block georeferencing is performed based approximated geotags information. That is the reason why, as previously mentioned, the mostly used low accurate sensor systems' measurement information don't provide enough accuracy in the direct georeferencing. Thus, a number of GCPs are required for the bundle block adjustment.

To do that, at least, three GCPs are introduced in image block orientation considering them as high priority observations in the least squares minimization (Nex & Remondino, 2013). These GCPs help in the determination of right 3D shape of the ground, correct eventual systematic errors as well as block deformations and absolutely orient the entire block in the ground coordinate system.

#### **2.5. Summary**

Nowadays, the use of UAV in aerial photogrammetry has apparently become so popular and very interesting tool for many applications. In this regards, this technology has won its reputation due to its very high resolution, manoeuvrability and low-cost hardware (Rosnell & Honkavaara, 2012). In recent years, this technology is spreading very fast all around the world, and so many types of research have been conducted in order to improve the quality of UAV products and meet at best the expectation of the users. So, it is in that motive that the current research has been conducted in order to develop and implement a reliable and efficient solution to the limitation in the traditional acquisition of GCPs used in the UAV image block adjustment.

### 3. PROPOSED METHODS

#### 3.1. Overview

The methodology adopted in this research project is subdivided into three main steps. Firstly, the quality in a geotag-based georeferenced UAV image block is analysed and assessed. Secondly, the manually selected control information from the aerial imagery is used for UAV image block adjustment. Thirdly, an automated approach to select and measure control points is developed and implemented and tested. The following drawings on Figure 3-1(a) graphically illustrate the scenario where a low accurate and deformed UAV image block is not well oriented as compared to the terrain. And on the same image, yellow vectors show how the 3D control points can be measured on the terrain along with corresponding points in both UAV image block. Also, an accurate orthophoto and DSM/DTM are showed with respect the terrain, whereby 2D points can be measured from the orthophoto and the height value taken from an elevation model and produce 3D point. These 3D points were later used to absolutely orient the UAV image block to the terrain. The drawing in Figure 3-1(b) shows how an adjusted UAV image block is oriented as compared to the actual terrain after the absolute orientation situation based on 3D GCPs.

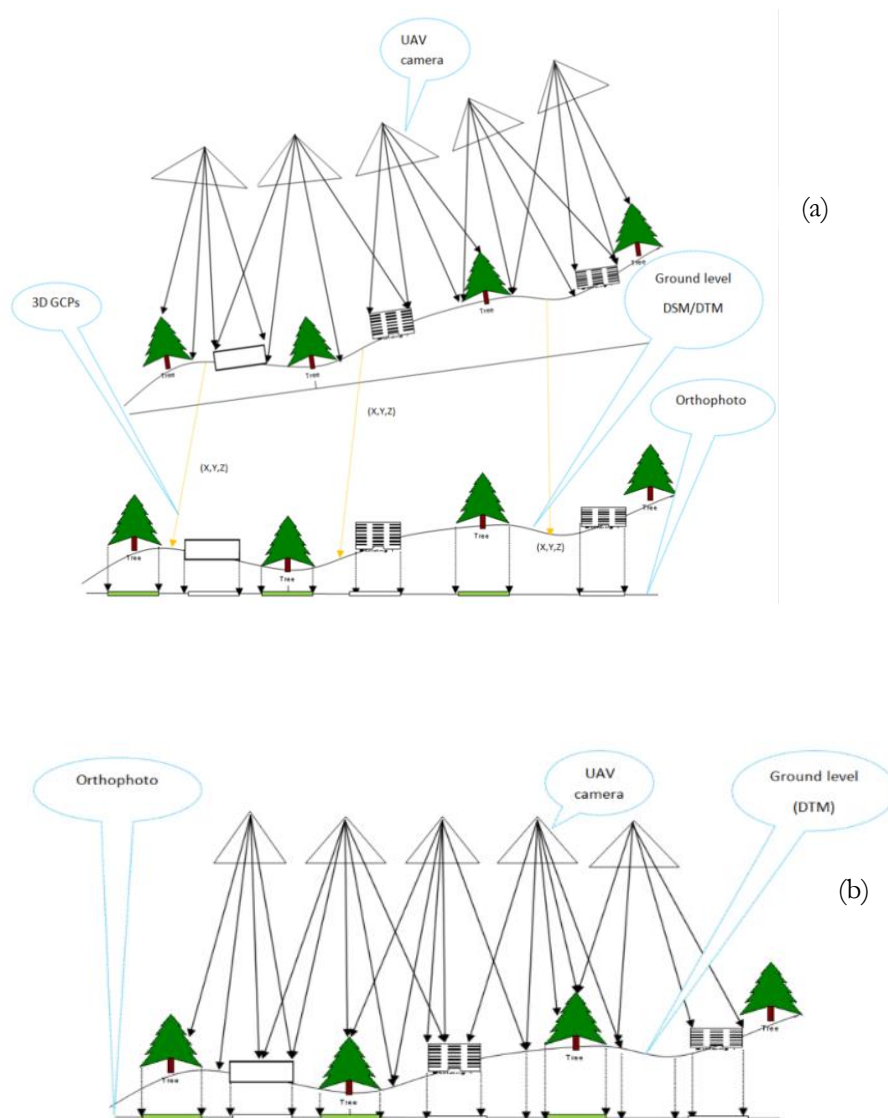


**Figure 3-1:** (a) Low accurate UAV image block with respect to the terrain; (b) Adjusted UAV image block and the terrain

### 3.2. UAV image-block quality assessment

The proposed UAV image block quality assessment is here presented in three steps. First, the image block absolute geo-location accuracy is assessed. Secondary, the detection and quantification of the image block deformation is also performed. Finally, the impact of different number and distribution of GCPs around the scene is evaluated. To do that, a set of accurate GCPs/CPs measured on the field is very essential, as well as a set of aerial photogrammetric products considered as additional reference dataset in this project.

#### 3.2.1. Workflow

This section presents the techniques used to assess the quality of the UAV image block. Thereof, for the implementation and evaluation of the proposed methods, the project experimental dataset described in Chapter 4.1 was used. Therefore, the same techniques were applied in assessing the quality in the image block oriented based on geotags only, as well as in case additional control points retrieved from external sources are used.

The following flowchart in Figure 3-2(b) illustrates the main steps of the above-mentioned process. And the symbols used in all flowcharts in this documents are defined in Figure 3-2(b). Whilst, Figure 3-2(a) presents the description of different symbols used in this project's flowcharts.

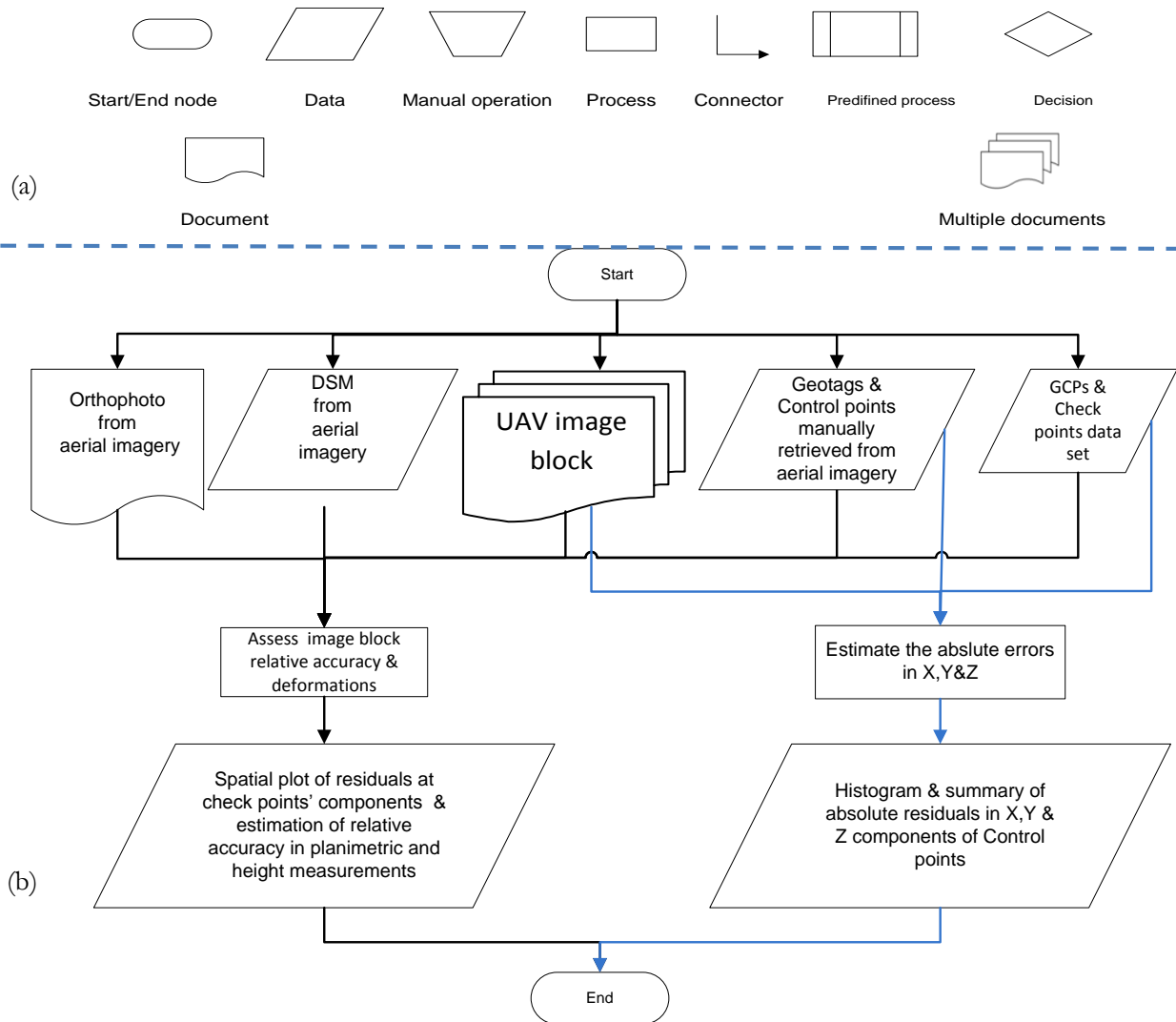


Figure 3-2: (a) Flowchart symbols; (b) Flowchart of processes for quality analysis of UAV image

### 3.2.1.1. Image block geo-location accuracy

The absolute accuracy in geo-location of the image bundle block is estimated using a number of high accurate and well-known Check Points (CP). This is done by analysing the residuals in  $X, Y, Z$  values in all the set of CPs in terms of Mean, Sigma and Root Mean Square Error (RMSE).

All these values are important in the analysis and presentation of the quality of the results of a given model compared to the observed ones. The mean and standard deviation present the spread of the outliers in a dataset while an RMSE present an average of the error in all the datasets.

Therefore, the mean, standard deviation and RMSE of the residuals are reported and interpreted based on the following formulas of geostatistics:

With  $(x_i - \hat{x}_i) =$  Distance between the reference and the measured values

**The mean error** is an average error at each direction component ( $X, Y, Z$ ). It is calculated by the following formula in Equation 3.1:

$$\mu = \frac{1}{n} \sum_{i=1}^n (x_i - \hat{x}_i)$$

**Equation 3.1:** Calculation of the Mean

**The Standard deviation**, also known as sigma ( $\sigma$ ) is calculated as a square root of the variance of a set of data, and is used to measure of dispersion of dataset. The following Equation 3.2 presents the formula used in the calculation of Sigma.

$$\sigma = \sqrt{\frac{1}{n} \sum_{i=1}^n (x_i - \mu)^2}$$

**Equation 3.2:** Calculation of the Standard deviation

The **Root Mean Square Error (RMSE)** of a set of data is a measure of total error defined by a difference between the real values (observed values) and the values predicted by a model. It calculated by the following formula in Equation 3.3:

$$\sqrt{\frac{1}{n} \sum_{i=1}^n (x_i - \hat{x}_i)^2}$$

**Equation 3.3:** Calculation of the RMSE

### 3.2.1.2. Manual image block relative accuracy and deformation assessment

In the UAV imagery quality analysis, relative accuracy and block deformation investigation are a very important factor because this factor has a negative impact on the quality of the derived photogrammetric products (Nocerino, Menna, Remondino, & Saleri, 2013). In this project, the mentioned study is one of the methods used to assess the quality of the direct georeference, as well as the results derived from indirect orientation methods. Hereof, the scatter plots of the residuals at the CPs and the points on the horizontal line on manmade objects were both used. First, the scatter plot were used to visually inspect the orientation of the modification based on the XY-vectors and Z-vectors of the residuals at the CPs. Then the horizontal lines on the constructions were used to assess the relative/local accuracy. But this manual method is only

recommended for very high-resolution imagery and measurements were taken on buildings that that are largely visible in an image frame. Basically, the scatter plot method is a very good because it clearly illustrates the magnitude and orientation of the deformations along  $X, Y, Z$  components as well as its distribution around the block extent most especially when a good number of well-distributed CPs is used. These details cannot be disclosed by traditional way of just using only the figures. Both methods were used in this project as it is going to be demonstrated in the following sections.

- **The deformation visualization**

The visual presentation of the image block deformation is one of the methods used in the quality analysis as explained above. In this case, the residuals at the CPs were plotted in the form of the XY-vector and Z-vector. Therefore, when there is a significant shift of the CPs in the horizontal space, that is indicated on the XY-vectors orientation and size. In the same way, the Z-vectors show the direction of the residuals in height. For interpretation of the output, the map scale provides the measurements units of the size of residuals on the scatter plot. In case the residual vectors have significant values and oriented in different directions from a certain region, it is a sign of block deformations in the concerned locations. And in case the residual vectors are oriented in one direction with a respect to a certain location that means that there is a systematic shift of the block. This is mostly observable in residual at CPs in the only geotag based oriented image block. Finally, when there are relatively small residuals in the  $X, Y, Z$  components of the CPs, the related vectors were also of minor values all around the extent of the image block. This means that the entire block has a good orientation with minor deformations. An example of spatial plot of residual at control points is illustrated on Figure3-3

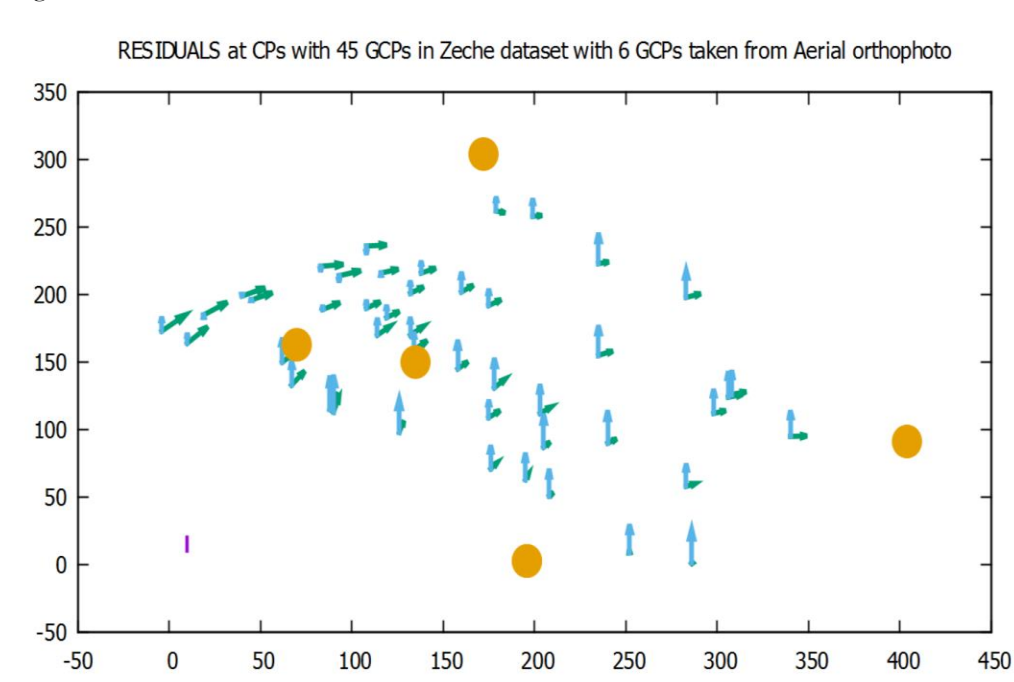


**Figure 3-3:** Example of the spatial plot of residuals at control points. Map elements: The purple bar for map scale of 10 cm on the ground; Yellow points for GCPs, Z-vectors in Blue and XY-vectors in Green.

- **Manual quantification of residuals in systematic rotation**

The quantification of residuals by residuals caused by systematic rotation was performed in terms of local accuracy, by calculating the difference in height between two points that are on the same horizontal line (Gerke & Nyaruhuma, 2009; Gerke, 2011). Theoretically, these points are expected to have the same height when measured in the same conditions. In the same way, the distance between the two points is measured and compared to the reference value measured in field or reference dataset. In this project, the reference dataset is image UAV image block adjusted with high accurate GCPs measured on the field. In this regard, the two points were measured in the ray-cloud of image 3D network, and the distance calculated using the Pythagoras formula for Euclidian distance. The Figure3-4 shows the way these measurements were taken. This process is to be performed in a number of manmade objects located in different areas of the image block in order to have enough samples for a better analysis on deformation state of the whole dataset.

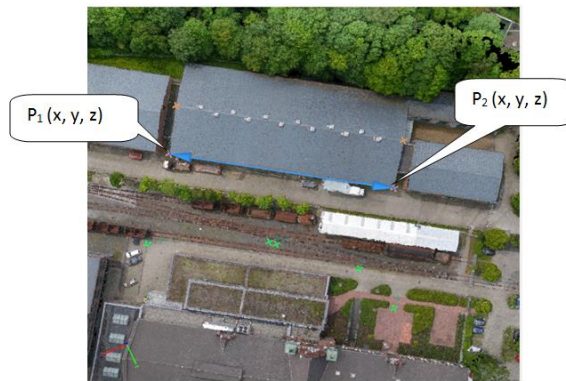


**Figure 3-4:** Quality assessment of a horizontal linear structure in a DSM of Zeche Zollern UAV dataset from ISPRS Benchmark from Multi-Platform Photogrammetry.

### 3.2.2. Impact of number and distribution of GCPs

In order to get a good accuracy in image bundle block orientation, the number and the distribution of the GCPs around the scene depend on the size and type of the topography of the terrain. In addition to that, it is also important to mention that the choice of the tools and technology used for the acquisition of the GCPs has a significant impact on the quality of the results and depends on the required positional accuracy for the intended purpose (Toutin & Chénier, 2004). This process is very important and has to be taken care of in order to get a good result.

In this project, the analysis of the number and distribution of GCPs is an essential step because it provides the information on the key factors in the quality of the results of a given block adjustment. Thereof, some configurations were implemented in the experiment datasets and the results were analysed. The summary of the results is presented in chapter 4.2.3.

### 3.3. Manual selection and measurement of control points

In this process, the main motivation is to reduce the cost of the indirect orientation of the UAV image bundle block for a better accuracy as explained in the first chapter. Therefore, the current research analyses the possibility of using available accurate aerial photogrammetric products in order to get necessary control information that would play almost the same role as ordinary GCPs. In this regard, the aerial orthophoto and elevation model are used as a source of control points' information. In order to implement that, the X and Y values were measured on points of the aerial orthophoto features that

are clearly visible on UAV orthophoto generated after initial process based on geotags only. This is a very important aspect, because, in most of the cases, these two image datasets (from UAV and airplane) were taken in different epochs, whereby, many changes are most probably available in the scene. Thereafter, the Z-value of the extracted points is taken from the elevation model. As a result, a set of 3D points were produced and used to improve the image bundle block relative and absolute orientation. In case only the DTM is to be used for height values, only the points that are measured on the terrain open-ground are considered. In contrast, when DSM is available, the Z-value of all the 2D points measured from the orthophoto can be measured and used for bundle block adjustment. In the following section, a workflow of processes for manual selection of control points is illustrated in Figure 3-5.

3.3.1. Workflow of processes

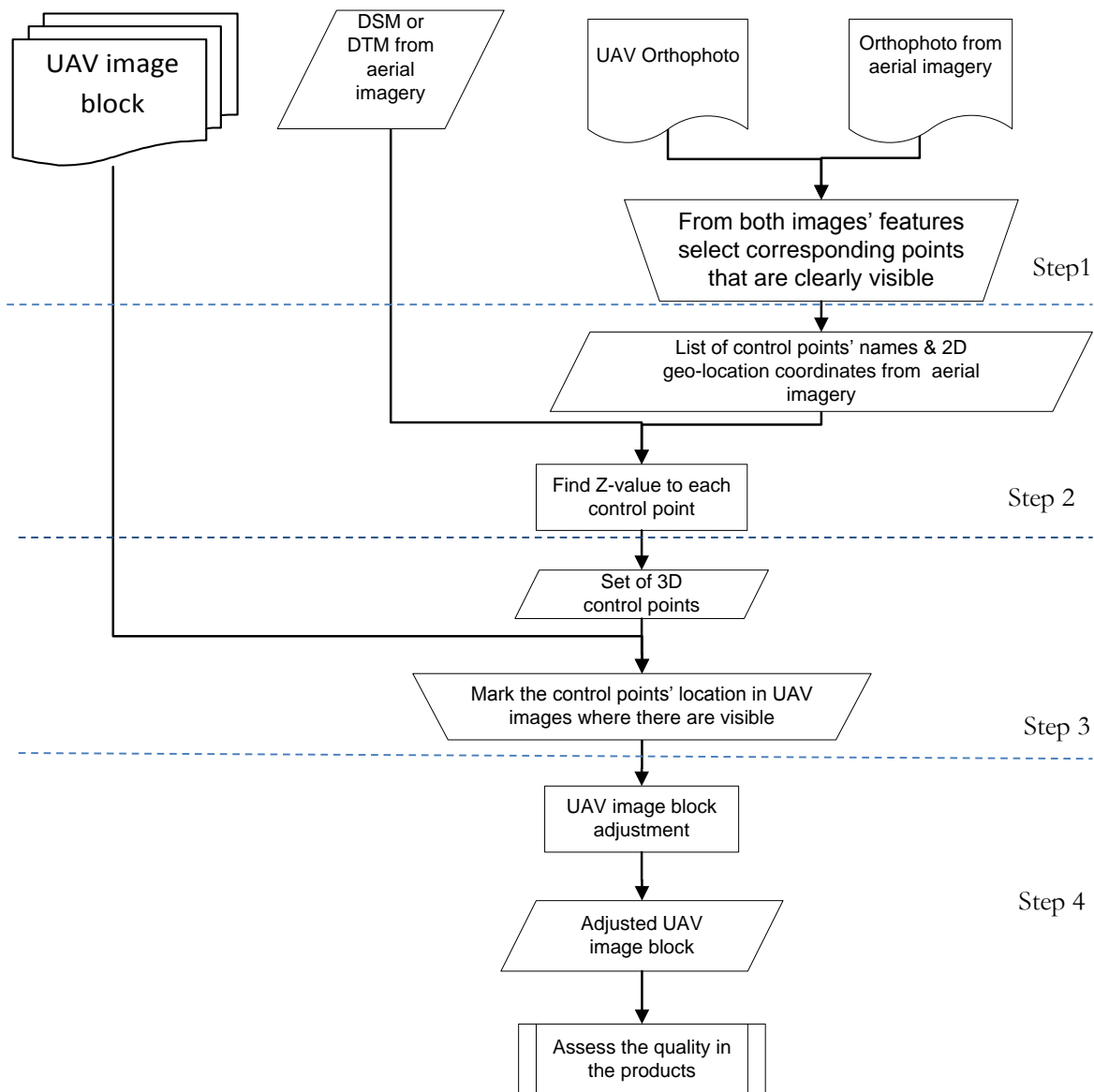


Figure 3-5: Overall workflow of processes of manual selection of control points from aerial imagery photogrammetric products

### 3.3.2. Workflow description and implementation

Based on the available UAV image block and orthophoto, as well as DSM and orthophoto from aerial imagery, 3D control points were manually selected and measured. Thereof, the above flowchart on Figure 3-5 illustrates four main steps of the processes applied in order to improve the accuracy of image bundle block orientation.

**Step 1:** Both UAV and aerial orthophotos are inspected and corresponding features are observed. Thereafter, in the aerial orthophoto, the points that are clearly distinguishable from its environment and visible in UAV orthophoto, are manually selected and considered as control points as illustrated in Figure 3-6. Then, each of these selected points' is labelled and assigned a 2D geographic coordinates of aerial imagery.

**Step 2:** Each of the measured 2D control points is assigned a corresponding height value (Z-value) taken from an elevation model of the aerial imagery. This done using any GIS professional software. In case only a DTM is available as elevation model, the Z-value is measured only for the points measured in aerial orthophoto of which corresponding points are visible on the open ground surface in the UAV orthophoto. As a result, a set of 3D control points is produced, loaded into the same system as the UAV images using a professional image processing software (Like Pix4d Mapper).

**Step 3:** For each of the control point, a corresponding pixel location is marked in every UAV image features where it is visible. This process is done in a professional image processing software.

**Step 4:** The entire image bundle block is adjusted and the quality assessed as described in the previous chapter.



**Figure 3-6:** Control points selection from aerial orthophoto on left side and UAV orthophoto on right side.

This process is one of the proposed methods to measure the control points that are used to increase the georeference accuracy of the UAV image. In this method, the control points are very good and lead to satisfying results when the user is skilled at visually recognize homologous features from two images of the same scene taken from different platforms and in different conditions such as position, time, scale and illumination. It only acquires attention in marking the point and it is advisable to zoom-in and select the right point in order to find a good result. In addition to that, the GCPs have to be evenly distributed around the scene in order to have a good result. The only limitation of this process is that in some cases it is not easy to find homologous points in both images because of various factors like different scales, illuminations, orientations. In this case, only a limited number of good points can only be selected with a risk of not finding a good distribution around the scene. However, this method is one of the possible approaches to increase the accuracy of the image block orientation and can considerably increase the quality of the UAV image block orientation as it is demonstrated in the experimentation results in Chapter 4.

### **3.4. Automatic selection and measurement of control points**

The UAV image block successful indirect orientation can only be achieved based on more accurate GCPs. Therefore, the second proposed possibility, is to programmatically find the control information from a more correctly georeferenced aerial imagery products of the same area.

In this project, another approach is developed, implemented and proposed, where a set of UAV images is co-registered to a more accurate aerial imagery orthophoto. Thereof, a number of control points must be measured from the master image (aerial orthophoto) and matched to the corresponding points in the slave image (UAV image) the same as way as in the above presented manual method. This is done using one of the computer vision community's algorithm to detect KPs and compute relative descriptors. Thereafter, these descriptors are compared and corresponding KP-pairs in both images are matched. However, as the KPs' selection is done image by image, in order to reduce the outliers in points' matches and reduce the unnecessary computational processes in the area outside the actual image space extent, it is a good idea to demarcate the new Area of Interest (AOI) in the orthophoto. After the demarcation of the new AOI of a specific image, an AOI buffer of 5 to 10 meters is set in order to compensate the eventual inaccuracy in the UAV direct georeferencing as illustrated in Figure 3-8 bellow. Finally, the orthophoto is cropped and the reference image is defined and used to find the KPs matching pairs that were used as control points in indirect UAV image block orientation. The process is iteratively repeated through all the entire UAV image dataset, and a list of control points is produced and saved in an Excel worksheet along with corresponding UAV image pixel locations and image names. In the following section, a summarized workflow of processes is presented.

#### **3.4.1. Workflow of processes**

In the following flowchart on Figure3-7, a workflow diagram of the main processes for a new proposed automated method is illustrated.

From Step1 to Step4, it is an iterative process that will be done through all the images of the UAV image dataset. Thereafter, the entire image block will be adjusted using the control information of the points measured in the previous steps.

A list of a sequence of UAV images' names and camera locations is read from an Excel Worksheet, which is one of the main input datasets for the application.

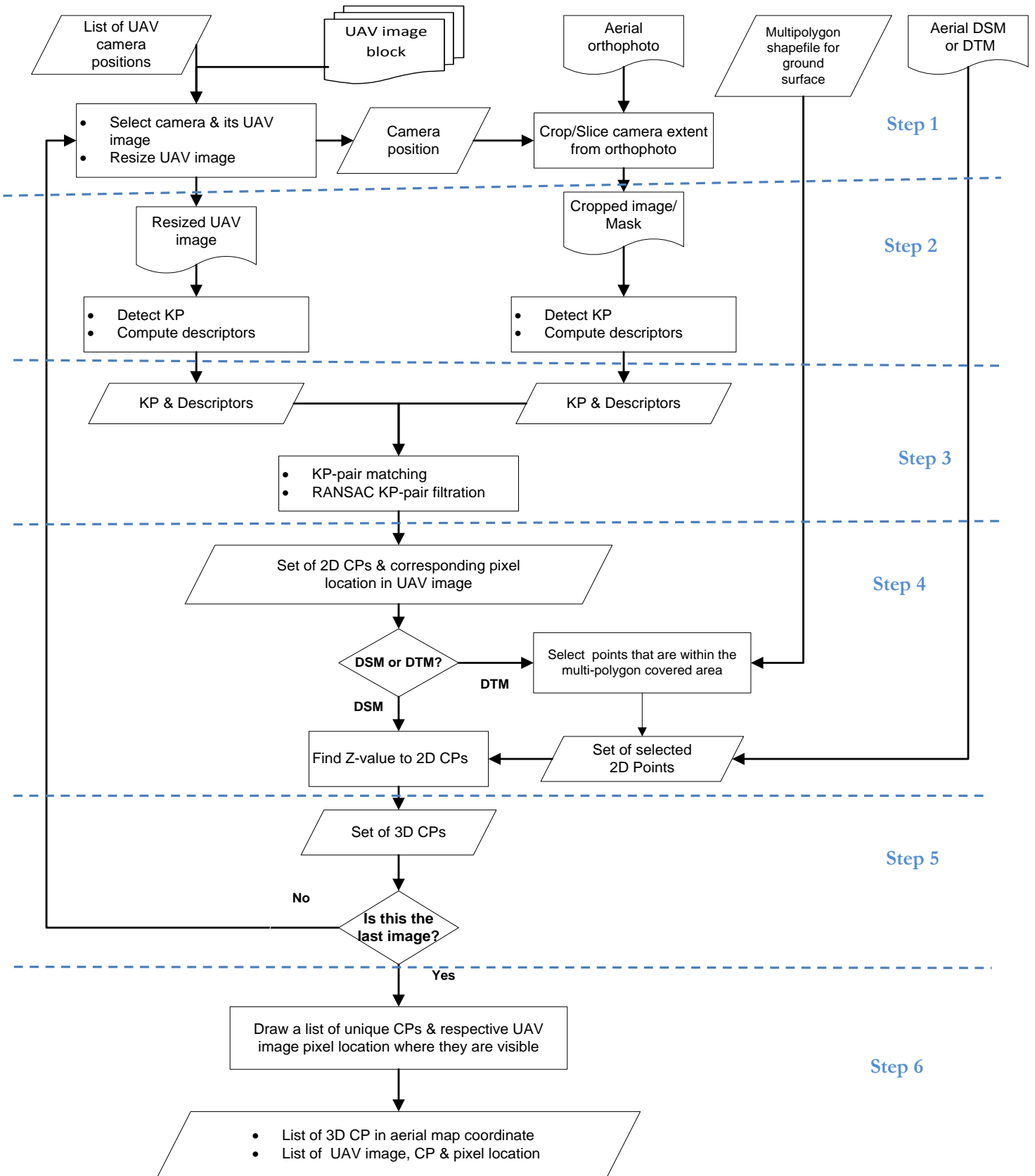


Figure 3-7: Flowchart of processes for automatically select control points from aerial imagery products

**Step 1: Select a UAV image and corresponding mask image from aerial orthophoto:**

In this step, first the application selects an entrée from the list of camera name and positions from an Excel Worksheet, then select the corresponding image from a file location where it is saved and resize it to the scale that is similar to the one of the aerial imagery. Thirdly, as the images were taken at nadir based on the camera position coordinates, a corresponding aerial orthophoto mask is estimated and cropped/sliced with a given buffer size depending on expected position error in the UAV direct georeferencing. This will increase the chance of having the UAV image spatial extent totally covered by the masked cropped aerial image extent. In this regards, the position of the corner points will be changed accordingly. In order to implement that, Table 3.1 illustrates the way the proposed algorithm estimates the UAV image extent in the aerial orthophoto pixel coordinates. Because the rotation parameters of the camera position by the time the image was taken are not known, the corners coordinates are just estimated based on known position of the UAV image center point. For more explanation, the image on Figure 3-8 provides more explanation of this process. As a result of this step, a resized UAV image and corresponding aerial orthophoto mask are produced and ready to be used for the selection of candidate control points.

The following is the aerial orthophoto masking process in order to determine a specific UAV image corresponding AOI:

- First, based on calculated image size and known pixel size, the positions of the 4 concerned pixels in the image space will be determined by  $x$  and  $y$  values. In this case, it is assumed that the image sides are parallel the  $X$  and  $Y$  axes of the aerial imagery projected coordinate system.
- Secondly, the minimum and maximum values in  $x$  and  $y$  coordinates of the set will be selected:

$$Min_x, Min_y, Max_x, Max_y.$$

- Thirdly the number of pixels needed to estimate 5 meters (buffer) on ground will be determined :  $n$

Finally, the new position of the end corners to the new AOI on orthophoto will be calculated following formula in the Table 3.1 below:

Point	Pixel position in the image
$P_a$	$(Min_x - n, Min_y - n)$
$P_b$	$(Min_x - n, Max_y + n)$
$P_c$	$(Max_x + n, Max_y + n)$
$P_d$	$(Max_x + n, Min_y - n)$

**Table 3.1:** The UAV image corresponding extent estimation from aerial orthophoto. With minimum and maximum values in  $x$  and  $y$  being  $Min_x, Min_y, Max_x, Max_y$ ; and buffer size in meters:  $n$

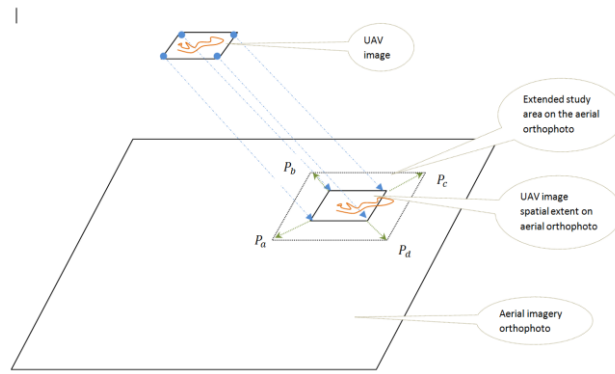


**Figure 3-8:** Limitation of the AOI for KPs detection and descriptor matching for one UAV image and aerial orthophoto

As the aerial orthophoto is georeferenced, the algorithm uses a geometry property detection function and finds the 2D coordinates of the top-left corner pixel as well as the pixel size (height, width). Then, from that information, the coordinates of a given pixel is calculated.

**Step 2: KPs' detection and descriptors matching**

At this step, two images are ready to be processed for the extraction of the ground control points. In this regard, SIFT or SURF or any other similar algorithm is used in both images, to detect KPs candidate for GCPs selection as it is implemented on OpenCV (2015). The expected output from this process is a dataset of 2D points. The following images on Figure 3-9 show the results of the KPs' detection in four UAV images and corresponding aerial orthophoto masks. After the KP detection, the algorithm will be also used to compute the descriptors of the selected KPs in both images. The images on Figure 3-9 show also the KPs' descriptors size and orientation of the gradients in the neighborhood.

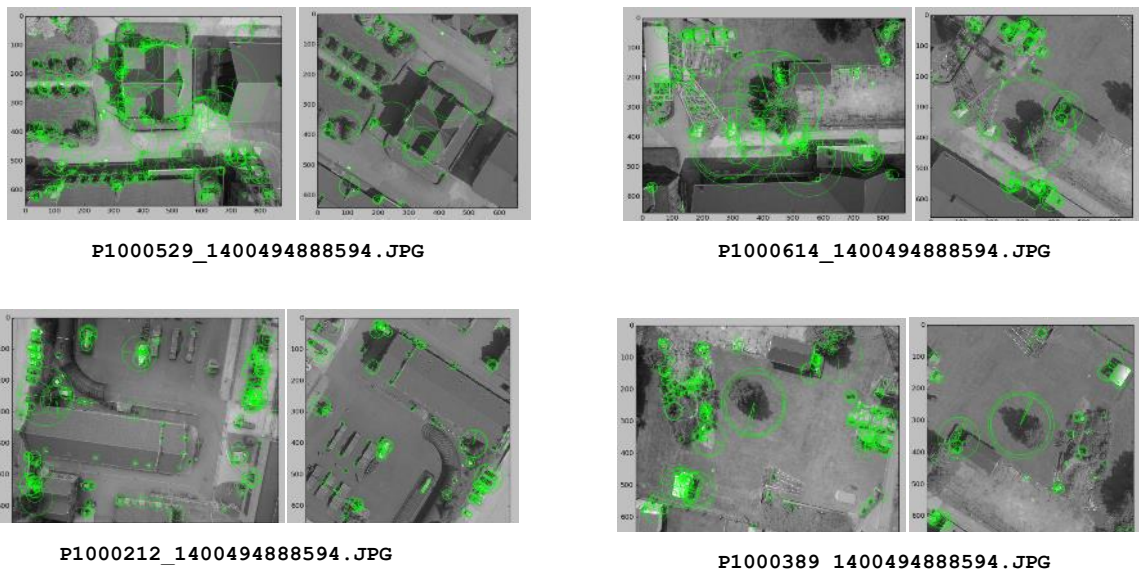


**Figure 3-9:** Example cases of SURF KPs detection and descriptors computation in UAV image (on left) and aerial orthophoto mask (on right). Green circles are KPs descriptors' illustrations showing the size and orientation of the change gradient of the pixels grey values in the detected KPs' neighbourhood.

### Step3: KPs descriptors matching and pairs filtration

The descriptors from both images will be compared and the application selects possible matching pairs based on the descriptors values and locations. The images bellow on Figure 3-10, show four examples of the KPs pair matches with Random Sampling Consensus (RANSAC) filtration on a threshold of 10.0.

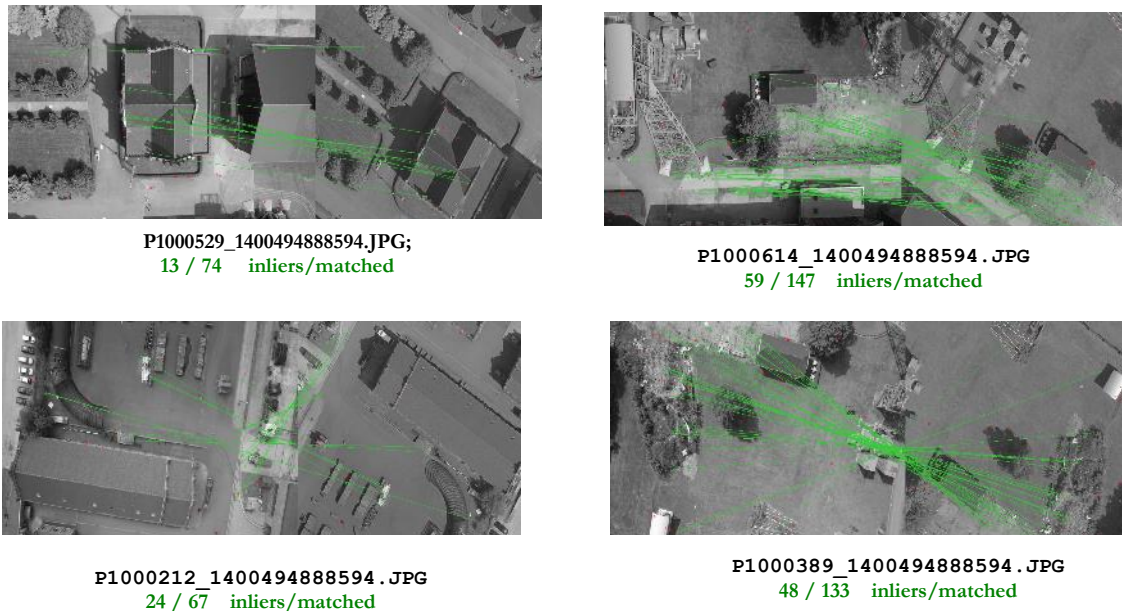


**Figure 3-10:** SURF KPs descriptors matching without any filtration. The green lines connects two corresponding points in both UAV (on left) and aerial image (on right)

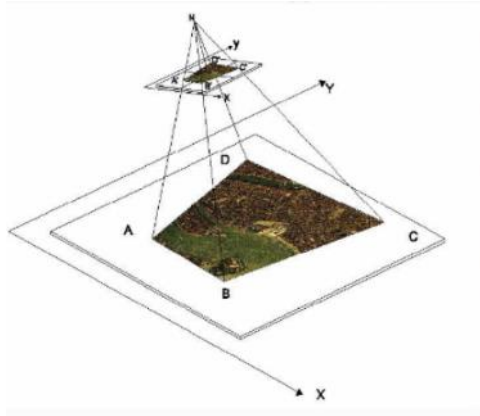
As it can be clearly seen in the image on Figure 3-10, SIFT or SURF algorithms are strong enough to detect the corresponding KPs without being interrupted with the variation in rotation neither the scale variation. This is illustrated by the connecting lines between two points that are in images of different rotation and scales.

#### Inlier and outliers detection

In the selected raw matching pairs from the previous process, RANSAC technique is applied to detect and eliminate the wrong matches. In this case, a homography transformation matrix is computed based on a minimum of four pairs and used to filter the inliers. This transformation is very well-known georeferencing technique and is based on geometric homogeneous coordinates and mathematic projective planes (CorrMap, 2015).

#### Homography transformation:

This projection is used in aerial photogrammetry where a map is assumed to be a perspective view of the observed ground surface as illustrated on Figure3-11. Then, the Formula 3.4 how the values of point are calculated in homography transformation. In this case, 8 unknowns parameters  $a, b, c, d, e, f, g, h$ , need to be determined in a form of the transformation matrix and used to estimate the corresponding points to the give points. Therefore, at least, 4 corresponding pairs are needed in order to estimate that matrix. In this project, based on raw matching points pairs selected from two images (UAV and aerial image mask), RANSAC technique is used to estimate the homography matrix and filter inliers from outliers. As a result, best matching pairs were taken as KPs (2D) from which GCPS in aerial imagery geo-coordinates will be measured, labeled and used for UAV image block adjustment.



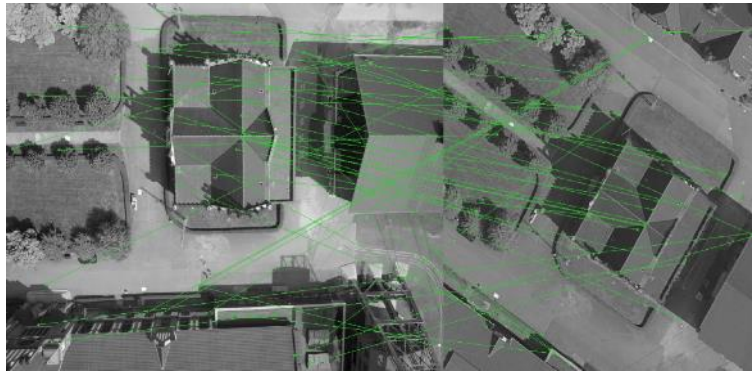
$$x = \frac{ax + by + c}{gx + hy + 1} \quad y = \frac{dx + ey + f}{gx + hy + 1}$$

**Figure 3-11:** Aerial photography where homography takes a map as perspective view of the ground; Source: (CorrMap, 2015)

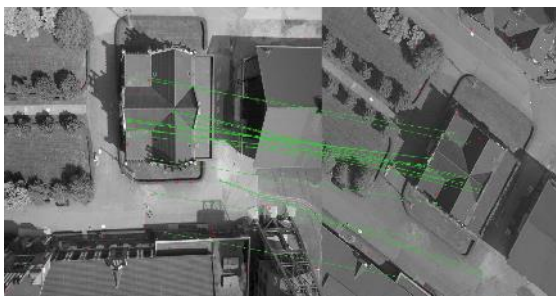
**Equation 3.4:** The homography transformation

### RANSAC:

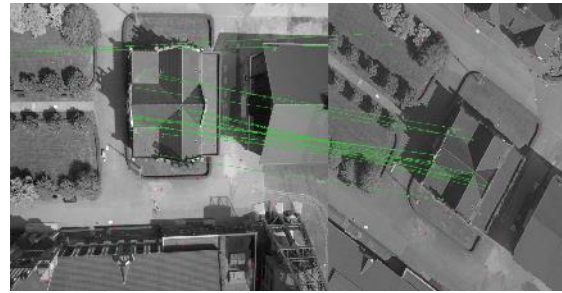
The Random Sample Consensus (RANSAC) is a technique which uses a minimum number of observations for the desired model parameters to generate candidate solutions to cope with outliers and inliers in a dataset (Derpanis, 2010). In this project, RANSAC will be used to analyse the geometric relationship in the KPs pairs measured in both master and slave image using SIFT KP matching algorithm and determine the good and bad matches. Consequently, this process needs to be carefully performed as if not performed well it may lead to bad results. As the UAV image and aerial image which are compared in this project are from different platforms, thus, different scale and perspective views, a high order transformation is required. To implement this process and expect better results, a projective transformation is used. As a result, a transformation matrix will be produced and used to exclude the outliers from a set of the KPs matching pairs. Considering that a minimum of 8 parameters is necessary for the homography projective transformation as presented in the previous section of this chapter, a minimum of 4 pairs of point matches is set as a starting data to instantiate the RANSAC process. This process provides an estimated homography transformation matrix from which inliers and outliers are determined at a given threshold. So, it is important to set the RANSAC matching threshold according to the image dataset in hand. Therefore, one must first of all visually analyse the matching filtration quality based on different threshold values. As a definition, RANSAC matching threshold parameter presents the maximum allowed projection error to treat a point as inliers (OpenCV, 2016). The following images in Figure 3-12 clearly show an example of different results of KPs' matches filtration in various thresholds.



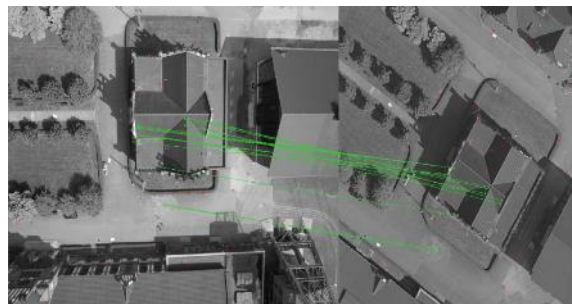
Raw KPs matches, 74 matched



RANSAC =20.0, 20 / 74 inliers/matched



RANSAC =10.0, 19 / 74 inliers/matched



RANSAC =5.0, 13 / 74 inliers/matched

**Figure 3-12:** Raw KPs pairs' matches between a UAV image P1000529\_1400494888594.JPG (on left) and aerial orthophoto mask (on right) with 73 matches; Examples of results of RANSAC matches filtration with different thresholds: 20, 19, and 13 inliers out of 73 matches for 20.0, 10.0 and 5.0 threshold values respectively; the green lines connects two corresponding points.

#### Step4: Find Height value to selected 2D KPs from an elevation model

At this stage, 2D GCPs dataset measured from the aerial orthophoto is available. The next step is the extract the corresponding height values from the available elevation model of the aerial imagery. Thereof, there are two types of expected elevation model. It can be a DSM or a DTM. Consequently, each case is processed particularly.

### 1) Case of DSM

In this case, the algorithm reads and automatically gets the height value from a DSM file based on 2D geo-coordinates of the concerned point. The result will be a list of 3D GCPs in aerial imagery coordinate system, ready to be used to indirectly georeference the UAV image block. These selected 2D control points were measured in all image feature without any distinction. That is because the DSM provides height values to all image features, be it ground and non-ground objects.

### 2) Case of DTM

- **Aerial orthophoto classification**

In case the only elevation model available is a DTM, the 3D points can only be determined based only on the points that are on the open ground. Therefore, both aerial and UAV orthophotos are visually inspected and the ground features that are visible in both images are demarcated from the aerial orthophoto. In addition to that, the image classification does not necessary have to cover the entire study area. Just a few strategically selected regions of the scene are enough. This is because the main objective is to find the some control points but evenly distributed around the scene to be used in the absolute orientation of the image block as explained earlier in chapter 3.2.2. Thereafter, a multi-polygon shapefile of the open ground surface is set in the same coordinate system as aerial imagery and used to get the KPs for which the Z value is measured from the aerial DTM. The flowing Figure 3-13 shows an example of a demarcated search area for KPs on the ground surface.



**Figure 3-13:** Aerial orthophoto ground surface classification for control points search area demarcation. Light yellow is demarcated search area; dark yellow rectangle is the boundary of the entire study area

- **Find Z-value to KPs**

After the selected KPs that are located in the area covered by the multi-polygon are defined, the corresponding Z-value is automatically taken from the DTM. The output is 3D control points which are considered as control points for UAV bundle block adjustment.

**Step5: Iteration through the list of images**

All the above steps, from step 1 to step 3, are performed on all the selected set of UAV images on the list as presented in Figure 3-14(a) and more clearly on Appendix 1. This list of images indicates also corresponding camera positions in the aerial map coordinate system. As indicated on the above flowchart in Figure 3-7, the application iterates through the selected images and continuously updates the list of control points and the image location where they are visible.

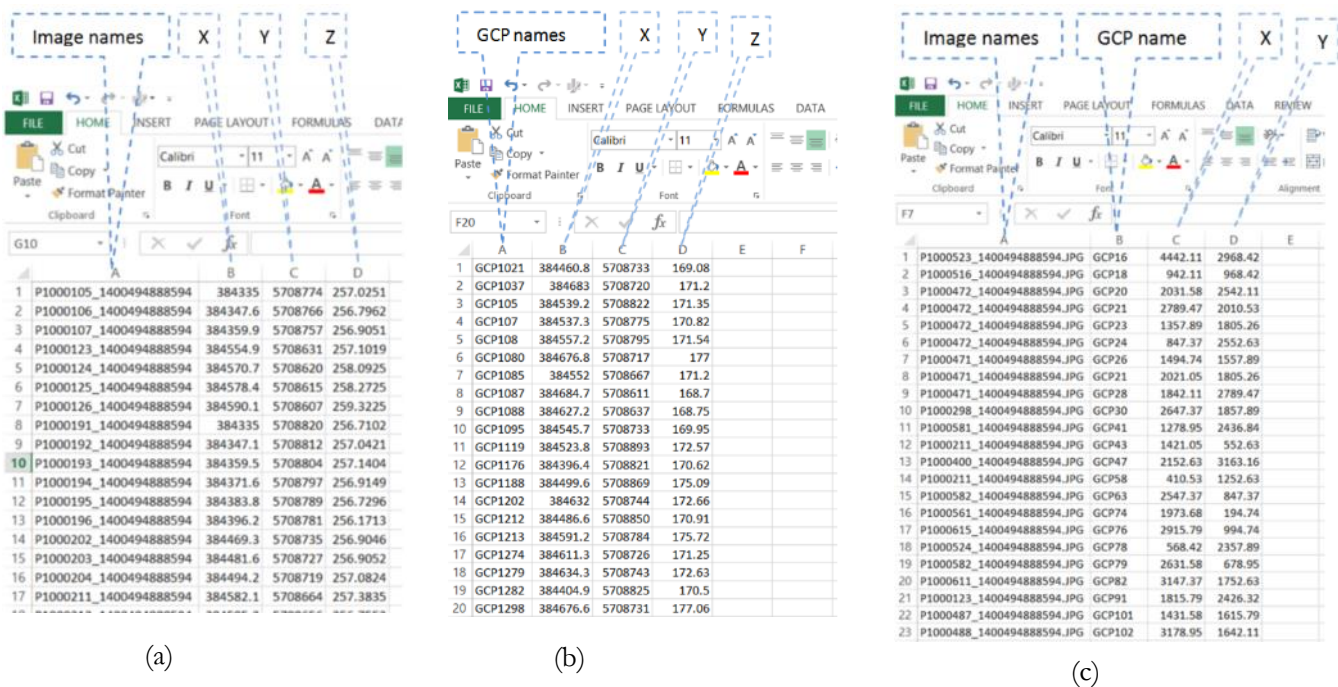


**Figure 3-14:** (a) List of images and corresponding camera positions; (b) List of selected and filtered unique control points; (c) List of control points and corresponding UAV image marks (pixel locations)

**Step6: Control points' datasets**

From previous steps, after the iteration through all the list of image cameras, a set of 3D control points is produced in aerial imagery coordinates as clearly illustrated above on Figure 3-14.(b) and Appendix 2. These points will be used later used as GCPs in bundle block adjustment. That is the reason why, for each control point, it is required to determine the corresponding pixel address in UAV images where it is visible. Therefore, the pixel coordinates of the points measured in UAV images are related to corresponding points in Aerial orthophoto map coordinates and generate two lists of the unsorted final set of control points with corresponding observation marks in the UAV images. Then a user-defined minimum number of images in which a control point must be visible so that it may be considered in further processes is used as a threshold to filter these control points. At this step, a final set of unique control points is determined based on their locations in the aerial map coordinate system and based on the given threshold of a number of images

where they must have corresponding pixels points, The results are saved in an Excel worksheet as described above in Figure 3-14(b) &(c) and more clearly shown in Appendix 2 &3.

### Step 7: Block adjustment

The dataset of 3D GCPs and corresponding point marks the location in images will be introduced in the entire image block adjustment process. At the end of this process, an oriented UAV image block is produced and tested for absolute and relative geolocation accuracy as well as checked for eventual deformations.

In summary, this is an automated method proposed to be used in the selection and measurement of control points that can serve as GCPs in the UAV image block adjustment. This method is effective and very efficient, as it requires minimum human labour in the control points selection, and measurements, as well as defining the basic corresponding points in the UAV images. The only required inputs are a set of UAV images, a list of camera position coordinates with corresponding camera names in an Excel sheet, a corresponding aerial orthophoto and elevation model. Thereafter, the application output is made of two datasets. One is a list of 3D GCPs' names and geographic locations and another one of each UAV image name, GCP name and corresponding pixel locations. Both results were saved in an Excel Worksheet and ready to be used in UAV image block adjustment using any image processing professional software. This algorithm can be implemented in any programming language using computer vision algorithm for KPs detection and descriptor computation. However, as most of the automated system, this algorithm needs the intervention of a human being for its best performance. This is mostly in setting the matching and filtration parameters, and some photogrammetric adjustment operations, like adding more GCP marks in images for a better accuracy in the results. Another drawback of this algorithm is the production of many KPs more than necessary. In this case, the application provides an option whereby a user can change a parameter as the minimum number of UAV images where a point in aerial orthophoto must have corresponding points. And this can be done when the initial selection did not provide enough or well-distributed control points around the scene. Otherwise, this algorithm, once it is well implemented, leads to good results as per the results of the experiments here presented in Section 4.4.

### 3.4.2. Implementation of the algorithm

In this project, the above-presented method was implemented and tested for efficiency. Thereof, a number of software applications and algorithms were used. And here follows a list of the main ones and their respective application in the current program.

#### 3.4.2.1. Software applications and libraries

##### Applications:

- **ArcMap:** This application is used for input data preparation, where the study area is visualized and strategic locations from where to select the cameras are demarcated. The result is a polygon shapefile from which the camera located within the area are selected and their names and coordinates saved in an Excel worksheet.
- **PyCharm:** This is an open source Integrated Development Environment (IDE) which used to program in Python. It is the main environment from where basically all the codes and library were implemented and run in this proposed automated method.
- **Microsoft Office:** By this application, Excel worksheet is used to write and read the list of the cameras for a specific location, as well as saving (storing) the output results.

##### Libraries:

- **OSGeo.Gdal: Open Source Geospatial Foundation (OSGeo)** is a library that has a number of packages like GDAL which was used in this project to read the geometry from a georeferenced raster image (GDAL, 2015).

- **CV2:** This is a package from Open Source Computer Vision (OpenCV) library (itseez, 2015). It provides programming functions that are used in this project for KPs detection and descriptors computation. One of its most famous function used in image photogrammetry for image feature detection and matching is SIFT (OpenCV, 2015b)
- **Numpy:** It is a library that is used for n-dimensional array objects(Numpy, 2013). This library is used very much in this project as the main type of data set that is processed are of raster type.
- **Matplotlib:** This is a library used in python interpreter for 2D plotting for data visualisation and exporting(MathWorks, 2016). In this project, Matplotlib was mostly used to visualize data in the KP pair matching for quality checking.
- **Xlsxwriter:** This is python library that is used to create and write in Excel worksheets (John McNamara, 2015). In this project, Xlsxwriter was used to read UAV image name and corresponding camera coordinates from a list on an Excel worksheet. In addition to that, this library is also used to create and write a list of selected control points and UAV images pixel locations where they have corresponding KPs.
- **PIL:** Python Imagery Library (PIL) is a library used in Python interpreter for image opening, processing and saving (Secret Labs AB, 2015). It reads many types of image formats and is open-source. In this project, this library is mostly used at reading, cropping and saving images during the execution of the process.
- **Shapefile:** This library is an open source product used in python to read and write ESRI shapefile GIS vector data (Lawhead, 2010). In this project is used to read the multi-polygon shapefile that masks the given search area for KP detection from a large raster image(orthophoto).

#### 3.4.2.2. Input data preparation

As illustrated in the flowchart of Figure 3-7, the application receives as main input a list of cameras, set of UAV images, aerial orthophoto and DSM or DTM. Hence, in the implementation of the proposed method, the developed application receives the list of cameras on an Excel spreadsheet, having names of images in the first column,  $X$ ,  $Y$ ,  $Z$  coordinates on second, third and fourth columns respectively. Then, for the set of UAV images, aerial elevation model and orthophoto, the application receives as parameters only the absolute paths to the location where they are stored. Therefore, the input data, have to be organized in order to meet the input data parameters properties and lead to the best results than can be achieved by the current application. In this regards, there are two types of application use, depending on the type of elevation model available. The first case is when a DSM is used for elevation measurements and the second one is the case of DTM. Basically, the two cases have different approaches, because, in the case of DSM, it is just a matter of limiting the number of UAV images, whilst for the DTM it the KPs which filtered in order to find those located on the ground surface.

- **Case of DSM**

In this situation, the method takes into consideration the principle of a good distribution of GCPs around the scene as presented in section 3.2.2. By that, the control points must be selected in different locations of the entire image block footprint. In addition to that, each GCPs must at be visible in at least 3 images. That is the reason why it is a good practice to demarcate strategic areas from where the control points will be searched in order to reduce unuseful points and speed up the execution of the process. Then the selection of the images is automatically performed based on geotags and demarcated area.

Figure 3-15 illustrates step by step how a list of the cameras is prepared before being used as an input parameter in case a DSM is used. The output is visualized in ArcMap and the final list is drawn and saved on an Excel worksheet as illustrated in Appendix 1.

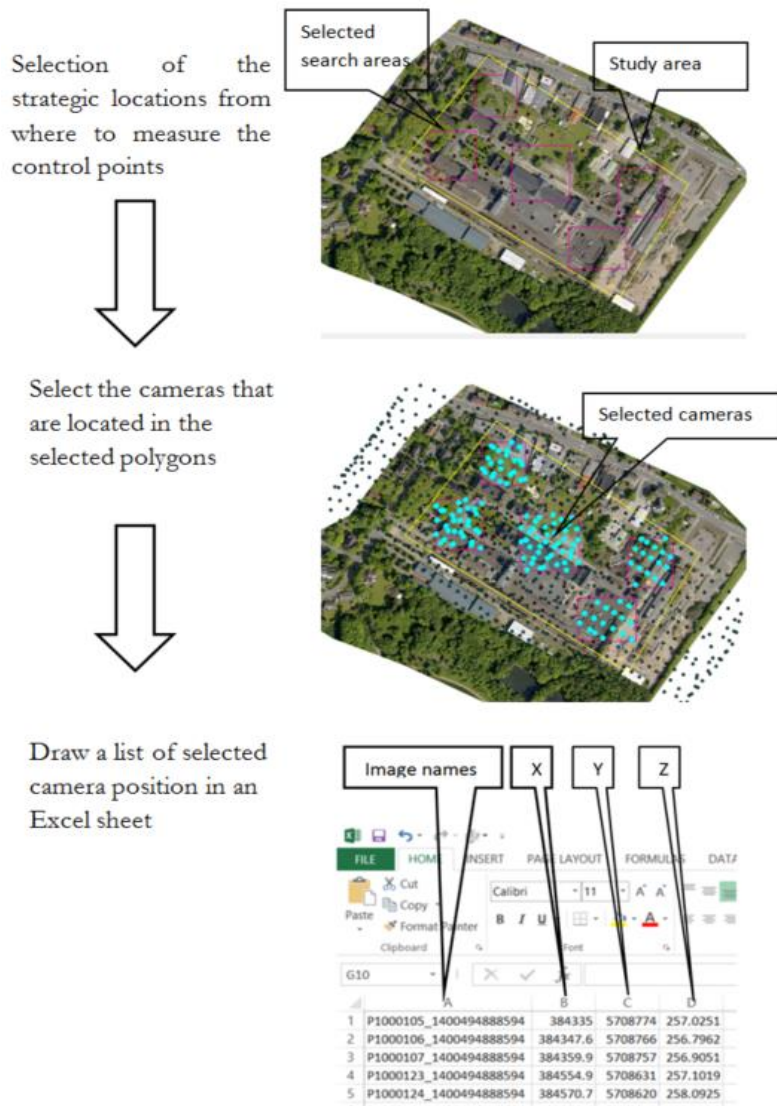


**Figure 3-15:** List of UAV camera data preparation in case a DSM is used as elevation model.

**Case of DTM**

In case the DTM is used as elevation model, the process is a bit different from the previous one. This is because, this time, not all selected 2D control points are converted into 3D points. In addition to that, the demarcation of the KPs' search area is only limited strictly to the open ground surface as explained above in the section 3.4.1. For more explanation, the following Figure 3-16 shows an example that illustrates clearly how the search area is delimited (masked) from the rest of the aerial orthophoto. It is also important to mention that, not all the not covered area has to be selected because the main objective is to find some points just needed for bundle block orientation as it has been the case in the previous section. So, the most important thing is to demarcate the areas around more or less all regions of the scene.

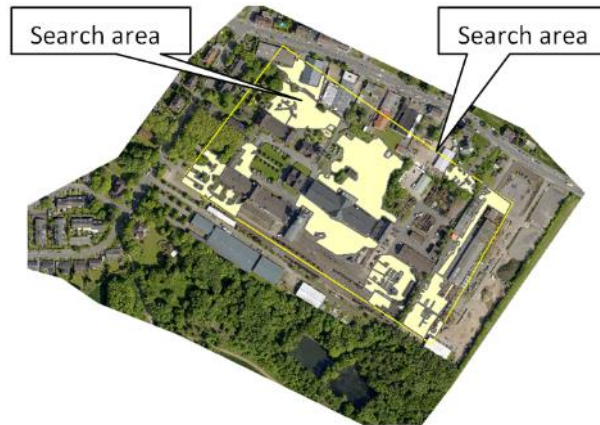


**Figure 3-16:** Demarcation for search area in case a DTM is used as elevation model. Yellow rectangular is the entire study area, and the light yellow coloured areas are the masked ground surfaces

After the demarcation of the search area, all the images of the entire projects are used for KPs detection compared with the aerial orthophoto. The resulting multi-polygon shapefile is used as one the inputs of the developed application program to select the control points that are located on the ground in the demarcated strategic areas for a good distribution around the scene.

### 3.4.2.3. Program execution

In the execution of the processes, the application follows a number of steps where objects of defined classes are called in a logical sequence.

The developed application was fully based on open source Python programming language and mainly openCV algorithms free accessible on the internet as tutorials (Intel Corporation, 2011). In this program, SURF technology was used to detect and compute the descriptors, due its processing speed as indicated in section 2.3.

The developed program provides the user with the freedom of changing the configurations depending on expected results and type of input datasets. The main parameter configurations a user can set are the following:

- **SURF parameters**

The user can change the number of pyramid octaves and layer taken in accounts while detecting KPs(OpenCV, 2015a). This is very important because, those parameters play an import role in detecting the KPs in images take in different atmospheric conditions, perspective, rotations and scale. The higher is the number of pyramid and layers the more selective is the application KP detection(Vedaldi, 2007).

- **RANSAC threshold parameter**

In order to find a perspective transformation between two images, a homography transformation matrix is estimated based on a minimum of 4 point pairs. In this project, cv2, FindHomography () function is used to find the matrix. This function has RANSAC as one of its parameters. Then RANSAC also uses a user-defined threshold to select inliers. This threshold is a float number with one decimal value and used as a limit size of allowed error in reprojection of a point (OpenCV, 2016). By changing that value, the user can visually check the accuracy matching patterns in a number of images and once it is sufficient, set it for the whole project.

- **Minimum number images per control point**

This application also allows a user to change the minimum number of images where a selected point must be visible so that it can be considered as a control point. This parameter is an integer value. It is an important aspect, because, in some cases, few points can be selected as having enough images where there are visible. In that case, a lower number can be set, and use a professional image processing software like Pix4d Mapper to manually mark the point in more images.

### 3.5. Summary

All the above-presented methods were expected to provide good results as much as they are well implemented. However, the quality of the results is assessed according to the intended purpose. But in most of the cases, the quality of the above two methods' results is reliable. This is confirmed by absolute residual values RMSE of around one-pixel size of the reference dataset in geo-location at CPs in the experimented sample dataset as presented in the next chapter.



## 4. RESULTS AND ANALYSIS

In this research project, Pix4D Mapper software was used to perform the initial process the UAV images and test the proposed methods' results. More details on this software can be accessed on Pix4D (2016). Hence, the initial image block is generated based on only geotags, then indirect orientation performed using control points from different sources as presented in this project. Therefore, in the following sections, different results are going to be presented and interpreted.

### 4.1. Description of experimental data

All the datasets used in this project are from ISPRS Benchmark from Multi-Platform Photogrammetry (Nex et al., 2015). From this benchmark, the data used in the project is composed of UAV images, aerial orthophoto and DSM, as well as a set of control points all taken at Zeche Zollern in Dortmund, Germany on 19th May 2014. Below on Figure 4-1, is an aerial image of the study area.

With respect to the acquisition type, UAV nadir images were taken by a Mavinci fixed wing airplane with a Panasonic GX-1 camera mounted on it on a GSD of 11 cm. Then, for the second dataset, the aerial imagery products were captured with PentaCam IGI flown by Aero West at a GSD of about 11cm.



**Figure 4-1:** The project study area, at Zeche Zollern in Dortmund –Germany;  
Source: (Google Earth Pro, 2016).

### 4.2. Data quality analysis processes

#### 4.2.1. Results of geo-location accuracy analysis

First, the image bundle block orientation from UAV direct georeference was assessed using high accurate and well-distributed CPs measured on the field. Therefore, after an initial image matching and bundle block orientation in a free network, the residuals on the CPs were estimated in all three components ( $X, Y, Z$ ). As it is demonstrated the results on Figure 4-2(a) and Figure 4-3(a), the UAV image block oriented based on only geotags, is the subject of some inaccuracy in both absolute and local accuracy due to the quality of georeferencing systems on board as explained in the first chapter. The statistics show an RMSE of about 2 meters in horizontal accuracy and 3 meters in height, with a mean error also that is about 2 meters, a half a meter and 3 meters in  $X, Y, Z$  components respectively. That means that the entire block has significant errors as compared to the ground truth that need to be corrected. That is also visually illustrated on the scatter plot in Figure 4-3(a) where the vectors of the residuals show a significant shift of the entire block in one 3D direction. However, this drawback can be compensated by the introduction of more accurate control points into the block orientation process. Therefore, as explained before, in most of the cases, the traditional way of using GCPs measured on

the field using high-end surveying tools are used and obviously provide the most reliable measurements if done by expert professional. But also, other sources of information can provide good control points that can serve in certain cases depending on the level of geo-location accuracy expected for a given purpose.

Thereafter, the UAV image block was adjusted using accurate GCPs and control points from the Benchmark as ground truth in this project. Then, the results were analysed for orientation accuracy and used as reference dataset when the products from other methods were discussed. In this regards, Figure 4-2(b) and Figure 4.-3(b) illustrate the geolocation accuracy summary in terms of absolute residuals at CPs when field measured GCPs and CPs were used.

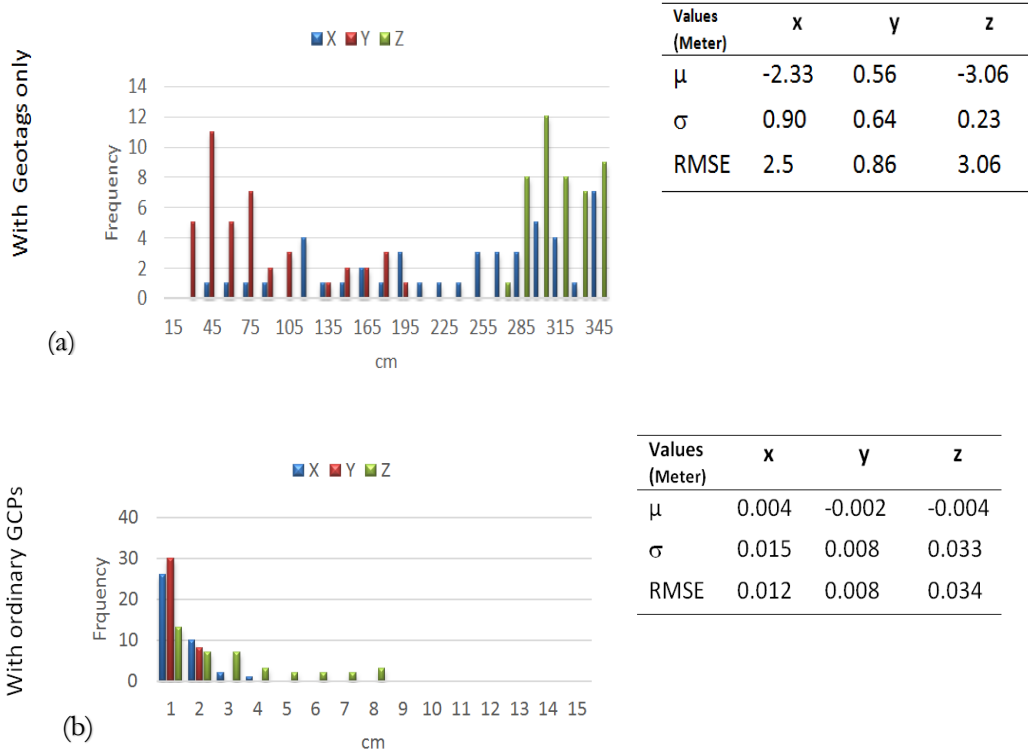


**Figure 4-2:** Absolute residuals at CPs (a) when only geotags are used and (b) When ordinary accurate GCPs were used

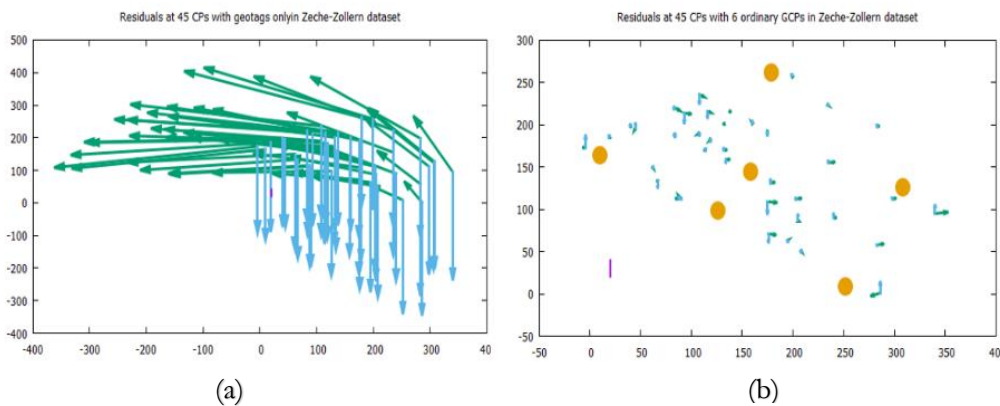


**Figure 4-3:** Spatial plot of residuals at CPs in X, Y, Z components in UAV image block (a) when only geotags were used and (b) when ordinary accurate GCPs were used. Purple bar is scale bar of 10 cm on ground, Green vectors are XY-residuals, and Blue vectors are for Z-residuals

**4.2.2. Results of manual quantification of residuals in systematic image block rotation or deformations**

The relative accuracy was assessed in terms of the image block deformation detection. As explained in the previous chapter, the points on two ends on a horizontal line measured on the edge of the roof of buildings were analysed in height difference and the distance between them as illustrated on images in Figure 4.4. In this case, the reference dataset is the results of the georeferencing of the UVA image block based well distributed and accurate GCPs. As it can be clearly seen in Table 4.1, for a geotag based georeferenced image block, in most of the points, the difference in height is significant as compared to the reference dataset, as well as the change in distance between two points. Then, on the same Figure 4.4, an overview of the quantity of the image block deformation is presented, and the errors in XY plane and Z-component are of 0.61m and 0.51m respectively. This is once again clearly visible on the spatial plot of residuals at CPs of Figure 4.4. Being that, the GSD of the UAV imagery in this data set is of 2.1 cm, this error is really big and needs to be corrected by indirect georeference using accurate GCPs.



**Figure 4-4:** UAV image relative accuracy assessment on the points on one horizontal line of features in the Zollern dataset.

Absolute residuals on Z-values				Relative errors in 2D space			
Object	Measured	Reference	Difference	Object	Measured	Reference	Difference
A	0.457749	0.008	0.449749	A	71.04848	70.323	0.72548
B	2.05457	0.12	1.93457	B	36.01028	35.343	0.66728
C	0.504456	0.072	0.432456	C	25.6810497	25.35	0.784974
D	0.027	0.135	0.108	D	67.05507	67.84	0.78493
E	0.16	0.033	0.127	E	38.791	38.852	0.061
Average(meters)			0.610355	Average(meters)			0.513947948

**Table 4.1:** Average estimation of deformation quantification of the UAV image block in Zollern dataset after the orientation using geotags only.

**4.2.3. Results on the analysis of the impact of number and distribution of GCPs in the image block**

In order to properly test and interpret the quality in the input data and outputs of the project implementation processes, the impact of the number and distribution of GCPs had to be inspected and analysed. This was done using ISPRS Benchmark of Zeche-Zollern in Dortmund /Germany, composed of 288 UAV images.

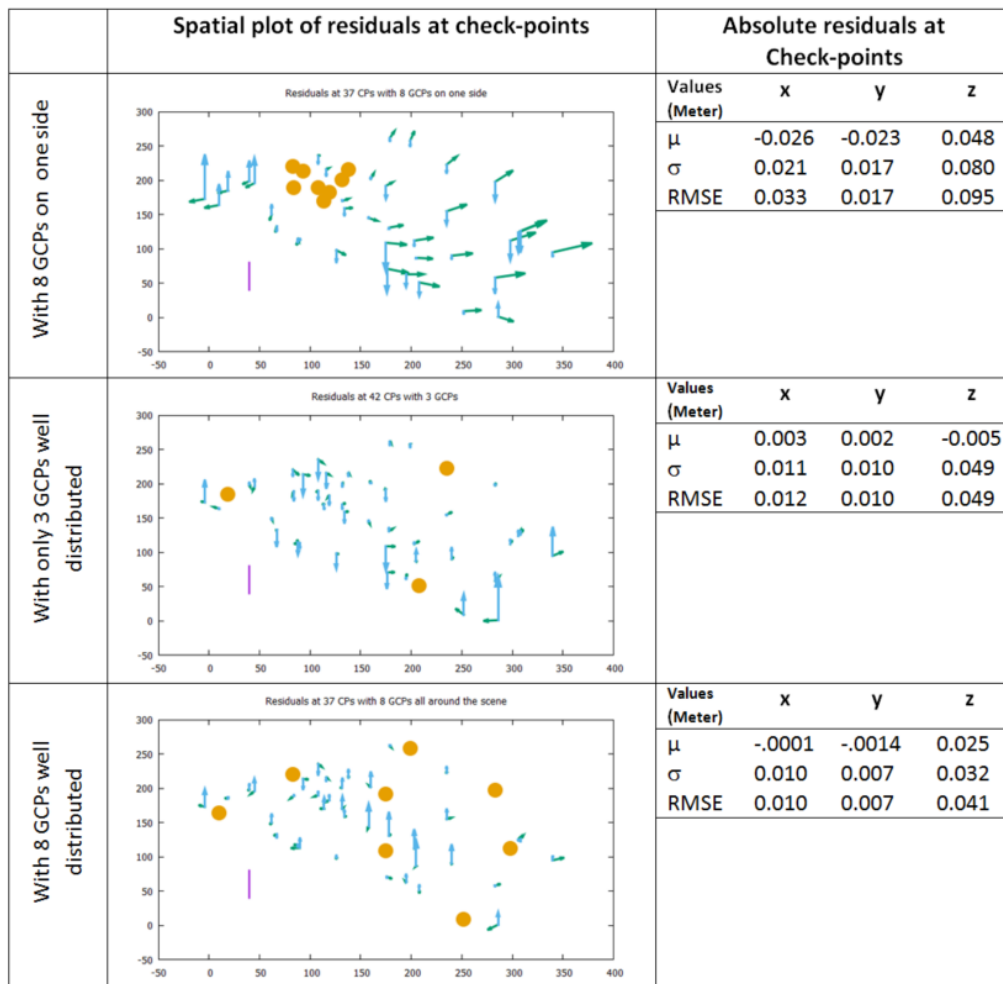


**Figure 4-5:** Residuals at CPs in X,Y,Z components in 3 different distributions of GCPs around the scene. Yellow points are GCPs and purple bar is scale bar of 40 cm on ground., Green vectors are XY-residuals, and Blue vectors are for Z-residuals.

Three types of configuration of GCPs and CPs were used for image block indirect orientation and analysed for quality in the results. First, 8 GCPs located on one side of the scene and 37 CPs were used to adjust the entire image block. Secondary, 3 GCPs and 42 CPs distributed all around the scene were used. And finally 8 well-distributed GCPs and 37 CPs were also used and all the results compared. As a part of the result, the above Figure 4.5 shows the impact of the distribution and number of GCP on the entire image block deformation illustrated by XY-vector & Z-vector of residuals at CPs and estimated absolute values of residuals in  $X, Y, Z$  components of CPs as well.

As it can be clearly seen on the above scatter plots, a number of GCPs, as well as its distribution around the scene, has an impact on the quality of the results. This is demonstrated by the first plot, where the GCPs are not evenly distributed around the scene and concentrated on one side, by the results in apparent deformation of the image block. In this case, all the vectors are oriented more or less in different directions from one location. This is a result of extrapolation where only points near the GCPs have low residuals as compared ones that are more distant.

In the second situation, 3 GCPs are used and distributed all around the scene. As a result, the block has fewer modifications as compared to the previous case. The modifications are there but not significant as in the first case, it is seen that there are fewer residuals in planar space than in height. This shows that the GCPS correct the deformations by interpolation with the points inside the covered area. In the third case, the modifications are fewer as compared to the two previous cases. That means, when a good number and well-distributed GCPs are used, good results are expected than otherwise. The interpolation of the observations values is more intense in the points inside the covered area.

In summary, as it can be clearly seen on the above Figure 4-5, the RMSE of the residuals at the CPs is very small in the case of an even distribution of the GCPs and increased considerably when the GCPs are concentrated on one side. This is also showed on the scatter plots, where the XY and Z residual vectors are very small in the area where the GCPs are distributed around the scene. This is a result of an interpolation in the points values inside the range of GCPs effect in the study area. On the other hand, the case where the GCPs are concentrated on one side of the study area, the XY and Z Residual vector are significant in the area a bit distant from the GCPs. This phenomenon is caused by the extrapolation effect.

From this, one can conclude that 3 or more GCPs evenly distributed around the a relatively small and flat study area leads to better results than in case they are only on one side of the scene extent. And the size and topography of the terrain are to be considered to strategically select the locations where to measure these control points.

### 4.3. Results of manually selected control points

Using the above-presented data, the method explained in Chapter 2 was applied to manually select the control points from aerial imagery products and adjust the UAV image block. In this section, these results of the experiment are presented and interpreted. In this project, Pix4d Mapper software was used to orient the images. Whereby, a set of six well-distributed 3D control points measured from the aerial imagery and the corresponding DSM was introduced in the UAV image block adjustment. And the quality was assessed based on residuals estimated from a set of 45 highly accurate CPs distributed around the scene.

First the summary of the results of geo-location accuracy analysis is presented, then the block deformation analysis' results are also reported.

### 4.3.1. Results of geo-location accuracy analysis

In order to test the efficiency of the use of the information manually measured from the aerial photogrammetric products, 6 control points measured in the same area as the field GCPs were used to orient the bundle lock and the results were compared.

As per the results reported in Appendix 4 and summarized in Figure 4-6, the proposed method is capable of increasing the accuracy in the UAV image block. This is demonstrated by a considerable decrease in RMSE in all components of the CPs. Whereby, the RMSE was reduced from 2.5m to 2.5cm, from 86cm to 4cm and from 3m to 40cm in  $X, Y, Z$  components respectively. The corresponding histogram shows that the average error in absolute values of residual that reflects how far of the measurements were from the observation, is of about 6cm in horizontal space, and all the measurement were less than 15 centimetres off from the observations. In addition to that, the spatial plot of residuals in Figure 4-7 shows a clear correction of the block shifts that were visible in the geotags based georeferencing results as illustrated in Figure4-5 above. As considering the reference dataset, which has a GSD of 11 cm, the accuracy of the results is of less than a half pixel size, which is tolerable in most of the cases. Therefore, this method can be considered as valid and be proposed as a possible solution to the UAV image block indirect orientation in case such level of accuracy is sufficient.

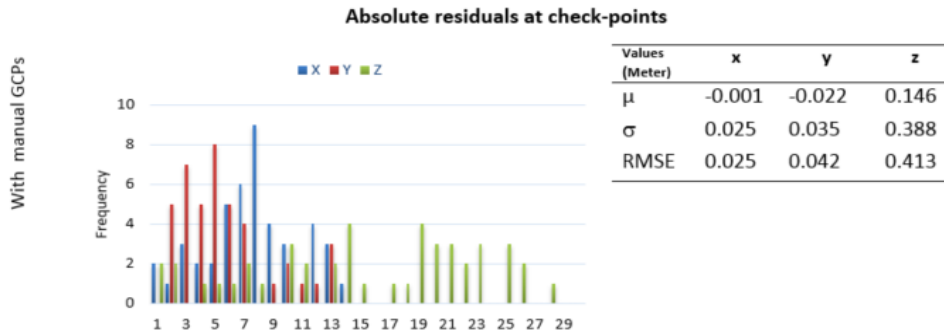


Figure 4-6: Absolute residuals at CPs when manually selected control points are used

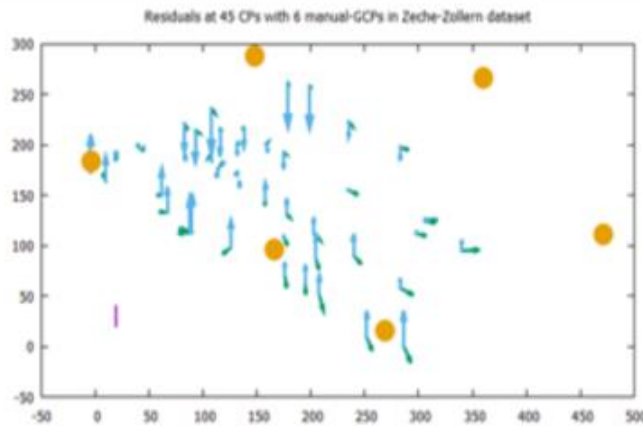


Figure 4-7: Spatial plot of residuals at CPs in UAV image block when manually measured control points are used. Purple bar is a scale of 10 cm on the ground, Green vectors are XY-residuals, and Blue vectors are for Z-residuals

#### 4.3.2. Results of manual image block systematic rotation and deformation analysis

The quantity of image bundle block deformation was assessed after indirect orientation based on 3D control points measured on the orthophoto and DSM of aerial imagery of the same area. The same process as explained in the previous chapter was applied in order to check the deformation in the block. Therefore, five objects were also explored and analysed in terms of relative accuracy. By this, the same points as in the previous sections were examined and the summary of the findings is presented in the following Table 4.2 following. In addition to that, the eventual deformation was also visually analysed using a spatial plot of residuals at 24 CPs. Finally, the results were compared to the ones of the orientation based only on geotags in order to find out whether the manually measured control points have managed to increase the accuracy in the UAV image block. The above Figure 4.7 illustrates the spatial plots of residuals at the CPs when manual control points were used.

Absolute residuals on Z-values				Relative errors in 2D space			
Object	Measured	Reference	Difference	Object	Measured	Reference	Difference
A	0.249	0.008	0.241	A	70.416	70.323	0.093
B	0.165	0.12	0.045	B	35.418	35.343	0.075
C	0.058	0.072	0.014	C	25.341	25.35	0.009
D	1.221	0.135	1.086	D	68.333	67.84	0.493
E	0.251	0.033	0.218	E	38.995	38.852	0.143
Average(meters)			0.3208	Average(meters)			0.1626

**Table 4.2:** Average relative error quantification of the UAV image block in Zollern dataset after the orientation using control points manually measured from an aerial orthophoto and DSM

Based on the above-presented results, there is an apparent improvement in the quality of bundle orientation, where the quantity of the deformations in the block was reduced to 50% (from 0.61 m to 0.32 m) and 30% (0.51 m to 0.16 m) in height and horizontal components respectively.

As it can clearly be seen, the manual control points have rectified the errors caused by the image block deformation, although it is not at the same level as the ordinary GCPs measured on the field with high-end professional surveying tools. On the second plot, one can see the large error in Z-component, this might be caused by the elevation model inaccuracy due to the values interpolation process which bears a certain level of errors. On the horizontal components, the XY-vectors has very small unfixed errors as it is also demonstrated by the statistics figures.

From the above results of the experiments where the manually selected control points from aerial imagery products were used to indirectly orient the UAV imagery, one can confidently conclude this method can be used to increase the accuracy in the UAV image block in case ordinary GCPs are not available. However, this process needs much attention, requires a certain level of proficiency in photogrammetry, and is also time-consuming. That is the reason why an automated method can be very beneficial to the users.

#### 4.4. Results of automatic selection of control points

In the previous section, a manual selection and measurement of control points from an aerial imagery was presented and the results were good as expected but still may be somehow cumbersome to some users. In this section, an automated selection of the control points was implemented as presented in chapter 3.4 in order to find a more efficient option as compared to the previously presented manual one.

As introduced in this chapter, the experimental data was acquired from an ISPRS photogrammetric benchmark of Zeche Zollern in Dortmund. As regarding the coding part, Python 2.7 and related image processing and computer vision algorithms were used as a programming environment. Thereafter, the

output of the developed application was used to indirectly orient the UAV image block using Pix4d Mapper software.

As it is presented above in chapter 3, the automated method was implemented in search way the process flow depends mainly on the type of elevation model available. In the case of the DSM, just the camera taken in consideration are selected, whilst in the case of the DTM, only the control points that are located on the opened ground surface are considered. Both cases were tested and the results are as follow:

**4.4.1. Case of DSM**

**4.4.1.1. Results of geo-location accuracy analysis case of DSM**

The geo-location accuracy has been also tested after the orientation of UAV image block based on generated GCPs from new developed automated method. As it is clearly illustrated in Pix4D Mapper report in Appendix 5 and summarised on the histogram of absolute residuals at a CP on Figure 4-8, the average error in the absolute location of the adjusted bundle block is about 1/3 pixel-size of the reference dataset in X & Y and two-pixel size in Z. And the histogram clearly shows that at most of the points, the errors are of less than 5cm off from the observations in the horizontal components and less 35cm in height components. That situation is also reflected in the spatial plot of residuals in Figure 4-9, where the XY-vectors are significantly reduced more that the Z-vectors. Therefore, one can consider these results as good because the main objective of increasing the accuracy in the image block has been achieved and at with least user manipulations. However, the application of a method depends on the intended purpose, so this method could be used in case a such a level of accuracy is satisfactory.

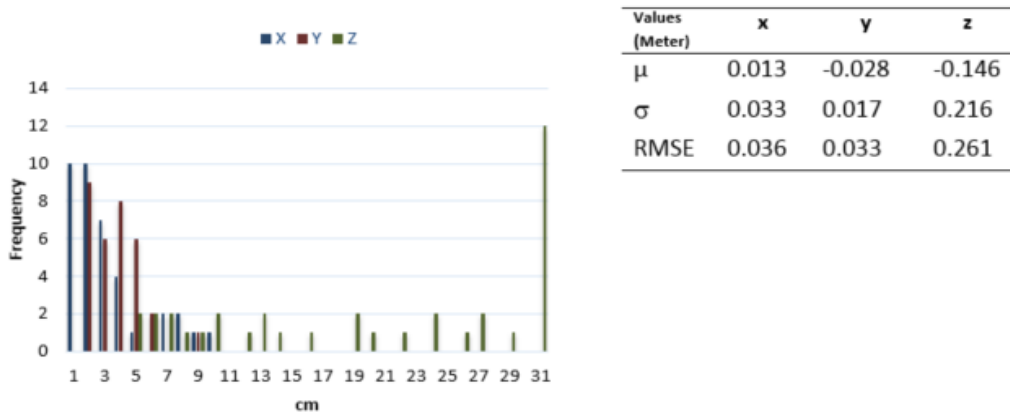
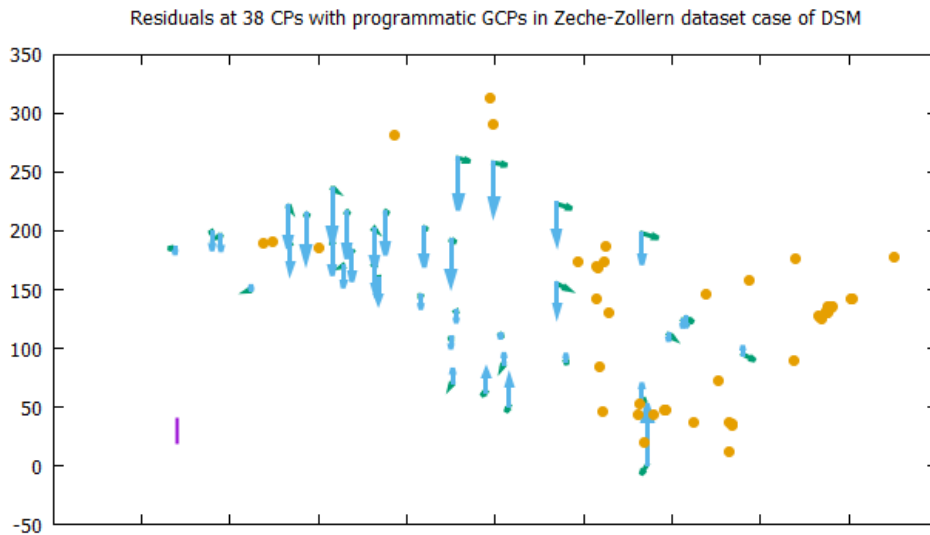


Figure 4-8: Absolute residuals at checkpoints when automatically selected control points and DSM were used.

**4.4.1.2. Results of deformation analysis case of DSM**

The results of the UAV image block adjustment based on automatically generated GCPs were assessed for accuracy. The results are presented in terms of block local and absolute accuracy.

Thereof, the block deformation was check visually by analysing the spatial plot of residuals at the CPs' Z, Y, Z components. As illustrated in Figure 4-9, the block has no apparent deformation, rather there is a minor shift of the entire block in one 3D direction. This is illustrated by Z and XY-components that are more or less oriented in the same 3D direction. In addition to that, by analysing the figures on the Figure 4-8, it is clearly seen that the entire block has an average of 2 cm residuals value in all CPs' components. This is about the 2-pixel size of the reference dataset.



**Figure 4-9:** Spatial plot of residuals at CPs in UAV image block when automatically measured control points and DSM are used. The scale is 1 bar is a unit of 10 cm on the ground, GCPs are yellow points, blue vectors and green are Z-vector and XY-vectors respectively.

#### 4.4.2. Case of DTM

In case a DTM is used as elevation model, the aerial and UAV orthophoto were visually compared and the surface area on the aerial orthophoto was demarcated as illustrated in Figure 3-14. The following results of the process applied to the experiment datasets. Thereof, all the images of the project were processed compared to the aerial orthophoto. The resulted control points were filtered to only select the ones that are located on the ground surface. The Figure 4-10 illustrates the location of the points around the study area and the corresponding location in UAV images. This is an example that illustrates the effectiveness of the algorithm in detecting and matching the control points in UAV and aerial images.

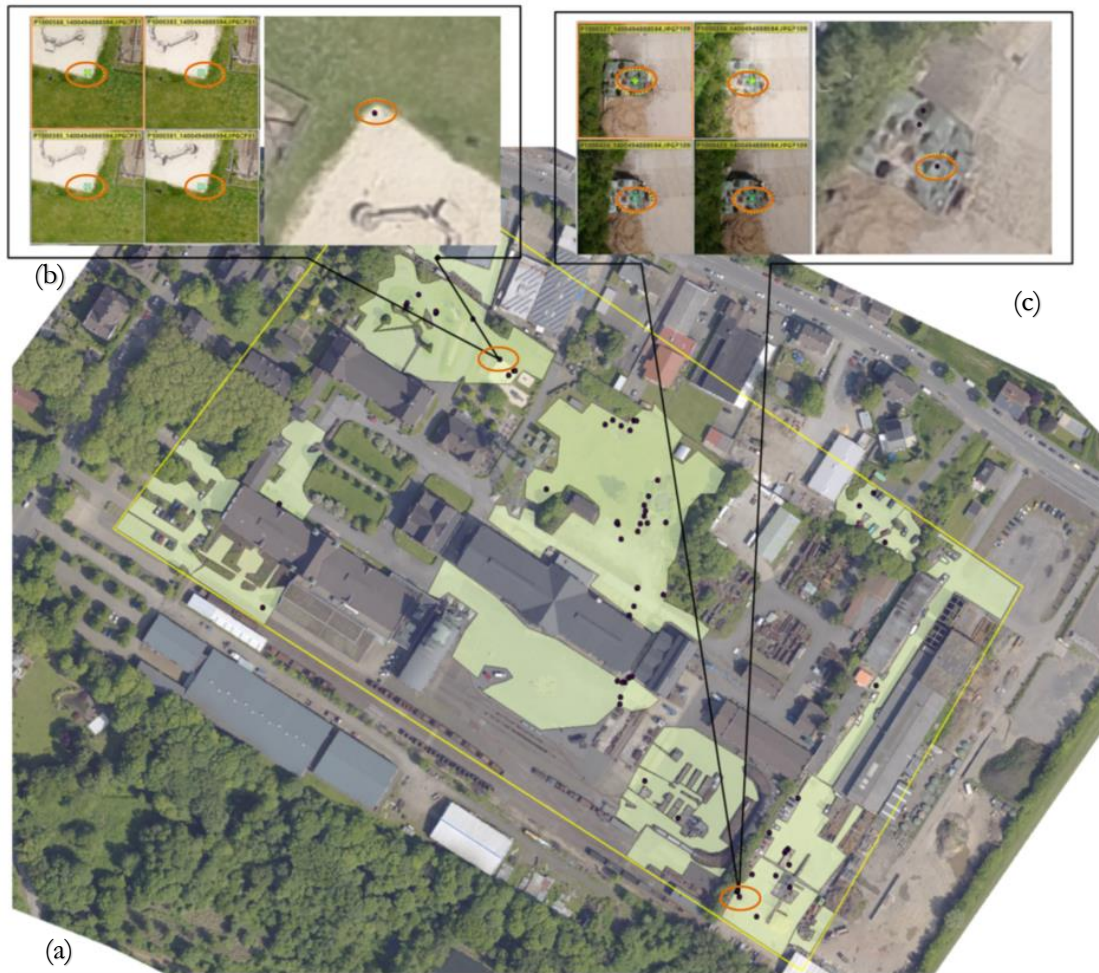


**Figure 4-10:** Example of results of control points selection when a DTM is used as elevation model. (a) The light green shows the masked area for control points located on the open ground surface. Dark brown points a selected control points resulted from the automated method. (b) & (c) Show in large two examples of selected points on the aerial orthophoto (Right side) and some corresponding UAV images where it is visible(Left side). The orange circle mark the selected control point.

#### 4.4.2.1. Results of geo-location accuracy analysis case of DTM

As it can be seen on Pix4d Mapper report in Appendix 6 and summarised on Figure 4-11, the geo-location accuracy of the image block after an indirect orientation has been increased considerably as compared to the initial situation. This demonstrated by the considerable reduction of the RMSE in all CPs components where it comes from 2.5 m, 0.85 m and 3.065 m to 0.085, 0.259 m and 0.141 m in  $X, Y, Z$  components respectively. That is a very good improvement. However as compared to the case where a DSM is used, it is not as good as that. That is probably to the limitation of the strength of the control points selected on the ground as compared to the ones on the objects above the ground. This limits also the even distributed expected while demarcating the search area around the scene.

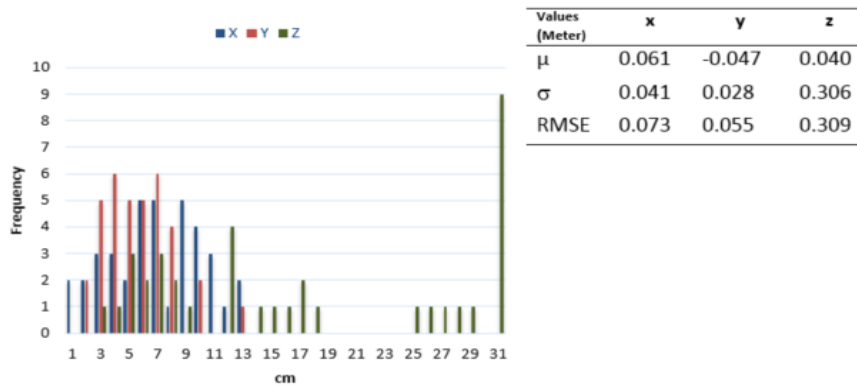


Figure 4-11: Absolute residuals at checkpoints when automatically selected control points located on ground surface were used.

#### 4.4.2.2. Results of deformation analysis case of DTM

This situation is a result of the above-mentioned impact of the control points as presented in the previous section. In this case, the image block has relatively small deformation but there is a visible shift of the entire block in one 3D direction which was not compensated by the control points as illustrated in Figure 4-12. That was probably because of weak distribution of control points around the scene and different technologies used to measure the height values in both UAV platform and CPs.

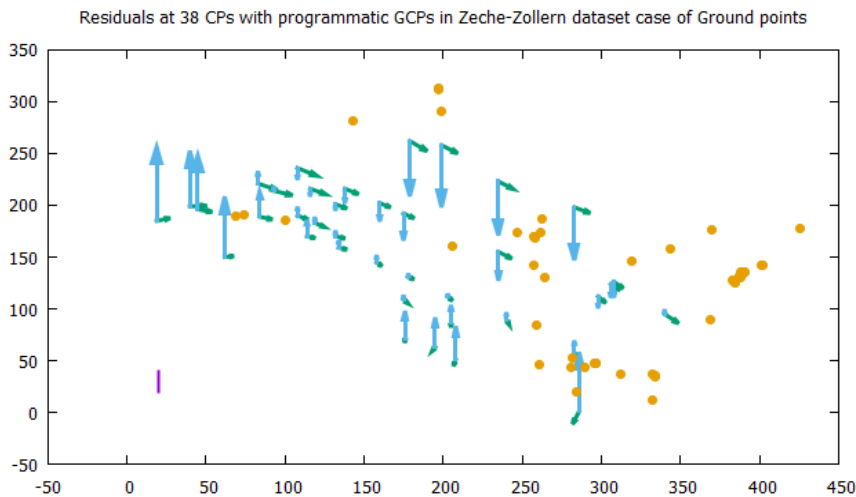


Figure 4-12: Spatial plot of residuals at CPs in UAV image block when automatically measured control points located on the ground surface only are used. The scale is bar is a unit of 10 cm on the ground, GCPs are yellow points, blue vectors and green are Z-vectors and XY-vectors respectively.

#### 4.5. Summary

In summary, the experimentations done using the available UAV imagery and aerial dataset as presented in this chapter has proved that the proposed methods can improve the accuracy of the UAV image block as expected. This is demonstrated by the results out of the implementation and test of both manual and automated methods which presented in above sections of this chapter. In order to have a general overview of the effectiveness of the new proposed methods, the results were summarized and compared with other ones from different types of direct and indirect georeferencing methods for UAV imagery of the same study area. Hence, the results of the current experiment were first analysed comparing them to results the geotags-

based UAV image block orientation as well as the results of the indirect orientation based on ordinary high accurate GCPs. Secondly, the new proposed methods' results were compared to the results of the two experiments carried out by Gerke & Rzybilla (2016) in the same study area where high-end and recent technology of RTK-GNSS enabled with 2-frequency receivers was adapted in UAV image inflight georeferencing and in case UAV cross flights were also performed.

#### 4.5.1. Case of direct georeferencing without UAV-based RTK

When compared to the UAV image block accuracy after direct georeferencing, the indirect orientation using all the three types of selection of control points has considerably increased the accuracy. This is clearly illustrated in Figure 4-13 where the residuals at CPs were reduced from more than one metre to more or below five centimetres in horizontal measurements and to around 20 centimetres in height measurements. In addition to that, when one compares the results of the new proposed methods and the case when ordinary GCPs was used, it is clearly seen that the late ones have obviously far better results in all components. But mostly, an apparent big difference is in height values, which is most probably because of the interpolation of values from a 21cm original resolution of the aerial digital elevation model to 2.1 cm in UAV imagery. But in XY components, the different is not that big as initial absolute errors in aerial imagery is in some extent propagated into the accuracy of the new control points measurements.

On the other hand, when the new methods are compared amongst them, the automated method where DSM is used has better results as compared to other two methods. This is likely due to the relatively better distribution of the measured points around the scene than the case when a DTM is used, and due to the high precision of points' selection when compared to the case of manual measurements. Generally, all the three proposed new methods have considerably and successfully managed to increase the accuracy of a directly oriented UAV image block.

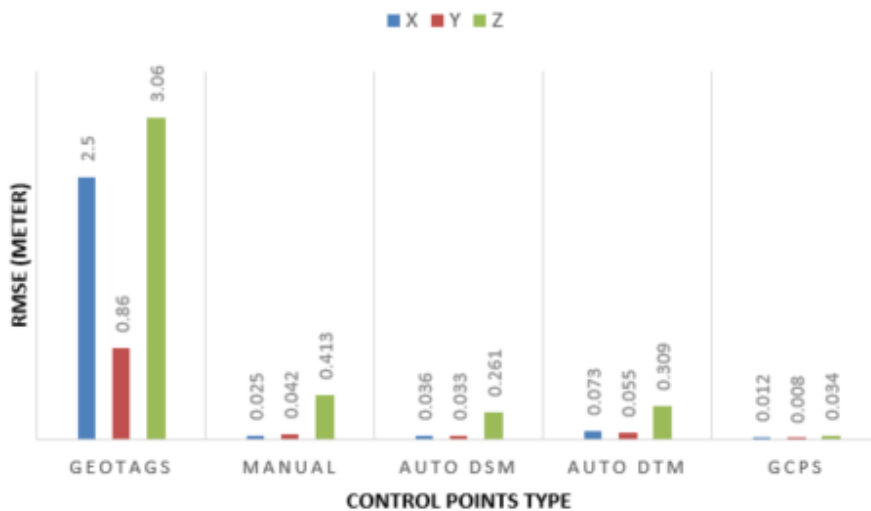


**Figure 4-13:** RMSE of residuals at CPs in X, Y, Z components, when different types of control points were used for indirect orientation of the UAV image block.

**4.5.2. Case of direct georeferencing with UAV-based RTK**

As introduced in above section, Gerke & Rzybilla ( 2016) have recently carried out an analysis of the influence of RTK-GNSS in UAV and impact of cross-flights on direct georeferencing. As the experiment was carried out in the same study area and using the same UAV aircraft platform, their results can be a good basis for the argument of the results of the current project.

On one hand, in the following Figure 4-14, a summary of the experiment results is presented in form of RMSE of residuals at CPs when UAV-based RTK is enabled. Whereby, in the left column cross-flight patterns were used and on the right hand, no cross-flight was used. And in both cases, the results of three configurations of GCPs are also presented. On the other hand, Figure 4-15 present the results of the current research whereby no UAV-based RTK is enabled for direct georeferencing, only three types of control points configurations were used for indirect orientation of the image block.

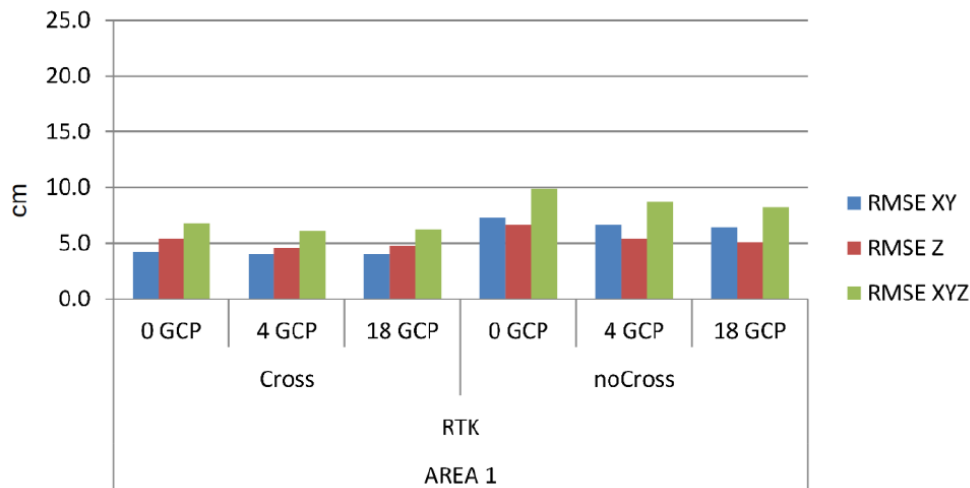


**Figure 4-14:** RMSE of residuals at CPs  $X, Y, Z$  components with RTK-GNSS enabled; on left cross-flight patterns are used, on right no cross-pattern used in 3 different configurations of GCPs; Source: (Gerke & Przybilla, 2016).

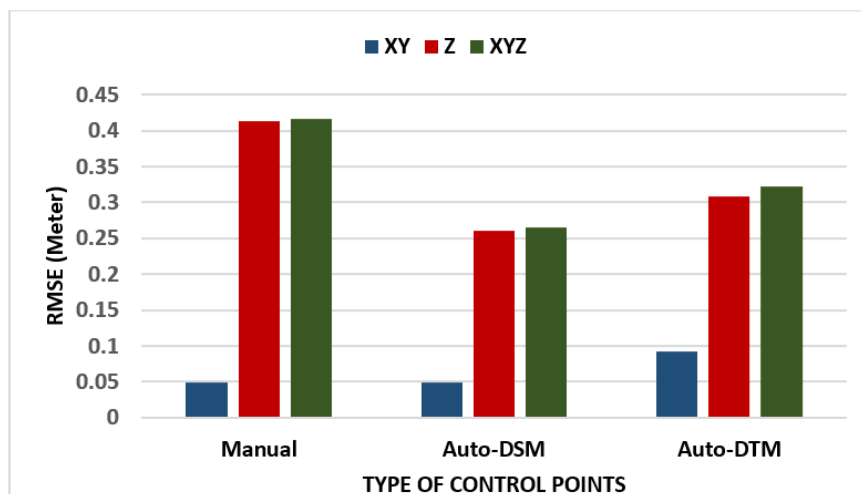


**Figure 4-15:** RMSE of residuals at CPs  $X, Y, Z$  components without RTK-GNSS and based on control points (From left to right) Manually selected with DSM, automatically selected with DSM, automatically elected with DTM.

Firstly, the above Figure 4-14 clearly shows that a UAV based RTK considerably increases the accuracy of direct georeferencing of the images whereby the errors in CPs at all components is more or less 5cm when

no GCPs were used. This is compared to the current research where no GNSS-RTK is enabled and the RMSE at CPs is of about 1.5m, 3m, and 2m in horizontal, height and 3D measurements respectively.

Secondly, the results of the indirect orientation of the UAV image block using new proposed method of selection of control points were used as illustrated in Figure 4-15 are compared to the ones in Figure 4.154. In this case, on a fast glance, one can see that in three new proposed methods (Manual, automated with DSM & automated with DTM) the accuracy in horizontal measurements is slightly better than the case where UAV-based RTK is enabled. But, the height measurements were far better in GPS-RTK system than in process based on aerial imagery orthophoto and elevation model. This is most probably because of errors produced by a height-value interpolation process from a larger GSD in aerial than in UAV imagery. Consequently, those large errors in height measurements make the errors in 3D become bigger in case the aerial orthophoto-based control points were used for bundle adjustment than in the case UAV-based RTK is enabled.

Therefore, the possible solution to the height measurement in the new proposed method can only be to use a highly accurate and high-resolution elevation model to estimate the Z-values to extracted 2D control points. Therefore, from this comparison, one can conclude that aerial orthophoto-based selection of control points can serve to increase the accuracy in the UAV image block in case GPS-RTK system is not available in the platform's sensor system. Hence, this analysis confirms once again that the new proposed method is reliable and can be proposed in various application where accurate aerial orthophoto and elevation model are already available.

## 5. CONCLUSIONS AND RECOMMENDATIONS

### 5.1. Conclusions

In this research project, two methods were proposed to indirectly orient UAV image block based on information extracted from larger aerial photogrammetry orthophoto and elevation model. At the beginning, the techniques used for image block quality assessment were presented whereby an absolute and relative accuracy were tested as well as the analysis of the impact of the number and distribution of the GCP around the scene. Secondly, using the datasets from ISPRS Photogrammetric dataset of Zeche-Zollern at Dortmund-Germany, the quality in the UAV image block oriented based only on the geotags was assessed in order to know the initial accuracy of the sensor systems on board. Thirdly, the same image block was adjusted by accurate GCPs measured on the field, and the results served as a reference to argue the results in the new proposed methods for ground truth acquisition. Finally, a manual and automated methods of acquisition of control points from aerial imagery were presented in details and implemented. Then, each dataset of control points produced by both methods was used to adjust the UAV image block, and the results were assessed for accuracy in the same manner as in previous processes. Generally, the results were good and the main objectives were met as expected.

In the case of the manual selection of manual selection of control points, the method managed to increase the accuracy in the UAV image at a level of more than 100 times which is of about a half GSD of the reference dataset (Aerial imagery). This shows that the method can be one of a reliable option to increase the accuracy of UAV image block, in case that level of accuracy can fit the mapping purpose. However, this method has limitations, since it requires advanced visual image analysis skills and point feature selection in different scales, illuminations and rotation. The main drawback is that in scenes where it is difficult to visually discern the image features like the areas where there are no man-made objects, the user risks to take wrong measurements or find few or not evenly disturbed points. In general, the proposed method is effective and can lead to reliable results once it is well implemented.

In case of the automated methods, the implementation yield relatively good results as expected, where the geolocation accuracy in the image block was brought from about two meters to around 3 cm in 2D space and from 3 meters to 20 cm in height measurement in case a DSM is used; and to also brought to around 7 cm in 2D space and 30 cm in height in case of a DTM. So, these results are relatively good for a fully automated process. This shows that once the processes were well implemented and the available aerial imagery is accurate enough, the method can produce reliable results. However, as most of the automated method, in order to maximize the quality, this method requires preliminary knowledge of photogrammetry so that necessary adjustments and proper setting of parameters as well as good preparation of input data can be well done. This is necessary by analysing the distribution of the produced control points around the scene, visually detecting and remove eventual outliers, and set the parameters according to the available imagery characteristics. In general, this method is very effective and can produce reliable results in the process of UAV image block adjustment.

As a conclusion, the accuracy of UAV image block can be increased based on control information measured from a more accurate aerial orthophoto and elevation model of the same scene. In this regards, the proposed manual and automated methods have been proved effective by providing considerably increased accuracy. So, the method can serve reliably in the case where such accuracy is needed and can fit the purpose. Furthermore, in some circumstances, both methods can be combined in case the distribution of the points automatically selected is not sufficient or manual selection of control points is not easy. Therefore, the main objectives of the current research were met, and research questions answered.

## 5.2. Answers to the research questions

### 1. What is the geo-location accuracy of the UAV image block direct georeferencing?

In the Section 2.4.1, the technique used to assess the absolute geolocation of the entire image block was presented and implemented on the available dataset. Thereafter, in the section 4.2.1, the results were illustrated in the histogram of absolute residuals at CPs and table of summary of residuals in terms of Mean, Sigma and RMSE. It was realized the image block had an average error of about one to three meters in  $X, Y, Z$  components.

### 2. How much deformation is in the available direct georeferenced UAV image block?

The proposed method to assess the relative accuracy and check eventual image block deformation was presented. And in using the project experiment dataset, this technique was implemented to analyze the quality of direct georeferencing. Then the results were illustrated in section 4.2.2 in the form of spatial plots of residuals at CPs and manual analysis of the residuals at the points on horizontal manmade objects. The results showed that the image block had a significant shift in one 3D direction which needed to be corrected by external control points.

### 3. How to manually find and extract homologous points from existing lower resolution aerial orthophotos and UAV images?

This question is answered in Section 3.3, where a new proposed method workflow of processes is illustrated and implemented. In this section, a full process pipeline is clearly described step by step with illustrations for more explanations. Whereby homologous points visible in both UAV and aerial orthophotos were visually detected, then manually selected and measured. At the end, a set of 2D control points were produced in aerial imagery map coordinate system.

### 4. How to get height values from available elevation model to 2D points selected as control points in both UAV images and aerial orthophoto?

Thereafter the production of 2D control points, the corresponding height values were taken from an elevation model. To do this, any case any GIS professional software can be used. In this case, a variety of GIS software professional application is available in commercial or free packages. For example, ArcMap, Erdas Imagine, Quantum GIS, ILWIS and some others applications as listed by The Institute For Mapping Technology (2010) and Statistical Consultants Ltd (2016).

### 5. How reliable and accurate is the use of the manually selected control points to perform the UAV image block adjustment?

As presented in section 4.3, the manually selected control points can considerably increase the accuracy in the UAV image block. The results showed that this method can reduce the absolute error up to about two UAV image pixel size, in case the aerial imagery is accurate enough. So, this performance can be useful in many cases where a such an accuracy can satisfy the mapping purpose.

### 6. How to automatically find and extract homologous points in both UAV image and aerial imagery photogrammetric products?

In section 3.2, the automatic selection of the control points from aerial orthophoto and available elevation model was presented, described and implemented. In this case, a fully automated method was proposed where a user just passes the input parameters to the application, and a list of 3D control points is produced along with corresponding images pixel locations. These two lists were ready to be introduced in the bundle block adjustment process.

### 7. **How can accurate UAV image block adjustment be achieved based on automatically detected and extracted control points from already available aerial imagery products?**

According to the results presented in section 4.4, this method is capable of increasing the accuracy up to about two UAV image pixel size. And this is a good result, which can be used in cases where a such an accuracy is sufficient. Therefore, the proposed method, once it is well implemented, can produce reliable control point, given the accuracy of the UAV image block orientation is even smaller than the aerial imagery GSD from which the points were measured.

### 5.3. **Recommendations**

In this research, the proposed methods for increasing the accuracy of UAV image block have resulted in satisfactory outputs whereas the main objectives were achieved. In contrast, due to the limited time, there are some points where this research did not reach that can be recommended for further studies, most especially in the automated method.

- Test the capability of reliably selecting the control points automatically in different environments, For example the rural area, forests and agricultural farms.
- To do a comparative analysis of effectiveness of different computer vision KP detection and descriptor matching algorithms in images of various resolution, with different cameras standards (professional or consumer grade) and draw a conclusion in terms of advantages and disadvantages so that a user can have an ease of selecting the one that can produce more reliable results in specific case. This should be tested in different UAV platforms, geo-positioning networks and Environments.
- A study on the use of high-resolution satellite images as a source of ground truth information for UAV image block adjustment. This is because, nowadays, recent satellite images are available almost in all regions and can be accessed at a relatively low cost.



## LIST OF REFERENCES

- Ahokas, E., Kuittinen, R., & Jaakkola, J. (2000). A system to control the spatial quality of analog and digital aerial images. *Eero Ahokas, Risto Kuittinen Juha Jaakkola, XXXIII*, 45–52.
- AIR-VID. (2015). 20 great UAV applications areas for Drones. Retrieved February 8, 2016, from <http://air-vid.com/wp/20-great-uav-applications-areas-drones/>
- Barazzetti, L., Forlani, G., Remondino, F., Roncella, R., & Scaioni, M. (2011). Experiences and achievements in automated image sequence orientation for close-range photogrammetric projects. *Videometrics, Range Imaging, and Applications XI*, 8085, 13. <http://doi.org/10.1117/12.890116>
- Barazzetti, L., Remondino, F., & Scaioni, M. (2010). Automation in 3D reconstruction: results on different kinds of close-range blocks. *International Archives of Photogrammetry, Remote Sensing and Spatial Information Sciences, XXXVIII*(Part 5), 55–61.
- Bay, H., Ess, A., Tuytelaars, T., & Van Gool, L. (2008). Speeded-Up Robust Features (SURF). *Computer Vision and Image Understanding*, 110(3), 346–359. <http://doi.org/10.1016/j.cviu.2007.09.014>
- Benigno, S. (2012). Geotagging images on mission planner. Retrieved January 20, 2016, from <http://www.marcusuav.com/geotagging-images-in-ground-control-software/>
- Berteška, T., & Ruzgienė, B. (2013). Photogrammetric mapping based on UAV imagery. *Geodesy and Cartography*, 39(4), 158–163. <http://doi.org/10.3846/20296991.2013.859781>
- Bolles, R., & Baker, H. (1987). Structure From Motion course. *International*, 1–49. Retrieved from <http://academic.research.microsoft.com/Search?query=structure+from+motion>
- Bone, E., & Bolkcom, C. (2003). *Unmanned aerial vehicles: Background and issues for congress*. Retrieved from <http://oai.dtic.mil/oai/oai?verb=getRecord&metadataPrefix=html&identifier=ADA467807>
- Chiabrando, F., Nex, F., Piatti, D., & Rinaudo, F. (2011). UAV and RPV systems for photogrammetric surveys in archaeological areas: Two tests in the Piedmont region (Italy). *Journal of Archaeological Science*, 38(3), 697–710. <http://doi.org/10.1016/j.jas.2010.10.022>
- CorrMap. (2015). The Homography transformation. Retrieved January 10, 2016, from [http://www.corrmap.com/features/homography\\_transformation.php](http://www.corrmap.com/features/homography_transformation.php)
- Derpanis, K. G. (2010). Overview of the RANSAC Algorithm. *Image Rochester NY*, 4(1), 2–3. <http://doi.org/10.1002/cne.901000107>
- EBee. (2015). The survey-grade mapping drone. Retrieved August 19, 2015, from <https://www.sensefly.com/drones/ebec-rtk.html>
- Eisenbeiss, H. (2004). A Mini Unmanned Aerial Vehicle (UAV): System Overview and Image Acquisition. *International Workshop on Processing and Visualization Using High-Resolution Imagery*, 7 pages.
- Eisenbeiss, H., & Zhang, L. (2006). Comparison of DSMs generated from mini UAV imagery and terrestrial laser scanner in a cultural heritage application. *International Archives of Photogrammetry, Remote Sensing and Spatial Information Sciences XXXVI-5*, 90–96. <http://doi.org/10.1.1.221.8350>
- Fgdc. (1998). Geospatial Positioning Accuracy Standards Part 3 : National Standard for Spatial Data Accuracy. *World*, 28. Retrieved from <http://www.fgdc.gov/standards/projects/FGDC-standards-projects/accuracy/part3/chapter3>
- GDAL. (2015). GDAL-Geospatial Data Abstraction Library. Retrieved November 12, 2015, from <http://www.gdal.org/>
- Gerke, M. (2011). Using horizontal and vertical building structure to constrain indirect sensor orientation. *ISPRS Journal of Photogrammetry and Remote Sensing*, 66(3), 307–316. <http://doi.org/10.1016/j.isprsjprs.2010.11.002>
- Gerke, M., & Nyaruhuma, P. (2009). Incorporating scene constraints into the triangulation of airborne oblique images. *ISPRS - International Archives of the Photogrammetry, Remote Sensing and Spatial Information Sciences*, 38(part 1-4-7/W5), on CD-ROM.
- Gerke, M., & Przybilla, H. J. (2016). Accuracy Analysis of Photogrammetric UAV Image Blocks : Influence of Onboard RTK-GNSS and Cross Flight Patterns. *Photogrammetrie - Fernerkundung - Geoinformation*, (1-2016), 14.
- Grenzdörffer, G., Engel, a., & Teichert, B. (2008). The photogrammetric potential of low-cost UAVs in

- forestry and agriculture. *International Archives of Photogrammetry Remote Sensing and Spatial Information Sciences*, 1, 1207–1213. Retrieved from [http://www.isprs.org/proceedings/XXXVII/congress/1\\_pdf/206.pdf](http://www.isprs.org/proceedings/XXXVII/congress/1_pdf/206.pdf)
- Gries, D., & Schneider, F. B. (2010). *Texts in Computer Science. Media* (Vol. 42). <http://doi.org/10.1007/978-1-84882-256-6>
- Haarbrink, R., & Eisenbeiss, H. (2008). Accurate DSM production from unmanned helicopter systems. *International Archives of Photogrammetry Remote Sensing and Spatial Information Sciences*, Vol. XXXVI, 1259–1264. Retrieved from [http://www.isprs.org/proceedings/XXXVII/congress/1\\_pdf/214.pdf](http://www.isprs.org/proceedings/XXXVII/congress/1_pdf/214.pdf)
- Han, Y. K., Byun, Y. G., Choi, J. W., Han, D. Y., & Kim, Y. I. (2012). Automatic registration of high-resolution images using local properties of features. *Photogrammetric Engineering and Remote Sensing*, 78(3), 211–221.
- Harwin, S., & Lucieer, A. (2012). Assessing the accuracy of georeferenced point clouds produced via multi-view stereopsis from Unmanned Aerial Vehicle (UAV) imagery. *Remote Sensing*, 4(6), 1573–1599. <http://doi.org/10.3390/rs4061573>
- Hemerly, E. M. (2014). Automatic georeferencing of images acquired by UAV's. *International Journal of Automation and Computing*, 11(4), 347–352. <http://doi.org/10.1007/s11633-014-0799-0>
- Intel Corporation, B. (2011). The OpenCV Tutorials 2.3.
- itseez. (2015). OpenCV (Open Source Computer Vision). Retrieved November 22, 2015, from <http://opencv.org/>
- J. Everaerts. (2008). The use of unmanned aerial vehicles (UAVs) for remote sensing and mapping. *The International Archives of the Photogrammetry, Remote Sensing and Spatial Information Sciences*, XXXVII(Part B1), 1187–1192.
- John McNamara. (2015). Creating Excel files with Python and XlsxWriter. Retrieved December 14, 2015, from <http://xlsxwriter.readthedocs.org/>
- Ke, F., Xie, J., & Chen, Y. (2016). A flexible and high precision calibration method for the structured light vision system. *Optik*, 127(1), 310–314. <http://doi.org/10.1016/j.ijleo.2015.09.178>
- Ke, Y., & Sukthankar, R. (2004). PCA-SIFT: a more distinctive representation for local image descriptors. *Proceedings of the 2004 IEEE Computer Society Conference on Computer Vision and Pattern Recognition, 2004. CVPR 2004.*, 2, 2–9. <http://doi.org/10.1109/CVPR.2004.1315206>
- Küng, O., Strecha, C., Beyeler, a., Zufferey, J.-C., Floreano, D., Fua, P., & Gervais, F. (2012). the Accuracy of Automatic Photogrammetric Techniques on Ultra-Light Uav Imagery. *ISPRS - International Archives of the Photogrammetry, Remote Sensing and Spatial Information Sciences*, XXXVIII-1/, 125–130. <http://doi.org/10.5194/isprsarchives-XXXVIII-1-C22-125-2011>
- Lawhead, J. (2010). Python Shapefile Library. Retrieved January 6, 2016, from <https://pythonhosted.org/Python Shapefile Library/>
- Leutenegger, S., Chli, M., & Siegwart, R. Y. (2011). BRISK: Binary robust invariant scalable keypoints. *Computer Vision (ICCV), 2011 IEEE International Conference on*, 2548–2555.
- Liu, B., Yu, M., Maier, D., & Manner, R. (2003). Accelerated bundle adjustment in multiple-view reconstruction. *Lecture Notes in Computer Science*, 11951201. Retrieved from <http://www.springerlink.com/index/8L868J36YV7LJQTP.pdf>
- Lowe, D. G. (2004). Distinctive Image Features from Scale-Invariant Keypoints, 1–28. <http://doi.org/10.1023/B:VISI.0000029664.99615.94>
- MarcusUAV inc. (2014). Geotagging Images in Ground Control Software. Retrieved January 20, 2016, from <http://www.marcusuav.com/geotagging-images-in-ground-control-software/>
- MathWorks. (2016). matplotlib. Retrieved January 11, 2016, from <http://matplotlib.org/>
- MAVinci. (2015). SIRIUS PRO Surveying UAS. Retrieved from <http://www.mavinci.de/en/siriuspro>
- Mostafa, M. M. R., Hutton, J., & Lithopoulos, E. (2001). Airborne Direct Georeferencing of Frame Imagery : An Error Budget. *The 3rd International Symposium on Mobile Mapping Technology, Cairo, Egypt*.
- Neitzel, F., & Klonowski, J. (2012). Mobile 3D Mapping With a Low-Cost Uav System. *ISPRS - International Archives of the Photogrammetry, Remote Sensing and Spatial Information Sciences*, XXXVIII-1/, 39–44. <http://doi.org/10.5194/isprsarchives-XXXVIII-1-C22-39-2011>

- Nex, F., Gerke, M., Remondino, F., Przybilla, H. J., Baumker, M., & Zurhorst, A. (2015). Isprs Benchmark for Multi-Platform Photogrammetry, *II*(March), 25–27. <http://doi.org/10.5194/isprsannals-II-3-W4-135-2015>
- Nex, F., & Remondino, F. (2013). UAV for 3D mapping applications: a review. *Applied Geomatics*, 6(1), 1–15. <http://doi.org/10.1007/s12518-013-0120-x>
- Nocerino, E., Menna, F., Remondino, F., & Saleri, R. (2013). Accuracy and block deformation analysis in automatic UAV and terrestrial photogrammetry - lesson learnt. *ISPRS Annals of the Photogrammetry, Remote Sensing and Spatial Information Sciences*, II-5/W1(September), 2–6. <http://doi.org/10.5194/isprsannals-II-5-W1-203-2013>
- Numpy. (2013). Numpy. Retrieved December 27, 2015, from <http://www.numpy.org/>
- Oh, J., Toth, C. K., & Grejner-brzezinska. (2010). Automatic Georeferencing of Aerial Images Using High-Resolution Stereo Satellite Images. *Isprs*.
- OpenCV. (2015a). Feature detection and Description. Retrieved November 25, 2015, from [http://docs.opencv.org/2.4/modules/nonfree/doc/feature\\_detection.html](http://docs.opencv.org/2.4/modules/nonfree/doc/feature_detection.html)
- OpenCV. (2015b). Introduction to SIFT(Scale-Invariant Feature Transform). Retrieved November 10, 2015, from [http://docs.opencv.org/master/da/df5/tutorial\\_py\\_sift\\_intro.html#gsc.tab=0](http://docs.opencv.org/master/da/df5/tutorial_py_sift_intro.html#gsc.tab=0)
- OpenCV. (2016). Camera calibration and 3D reconstruction. Retrieved January 3, 2016, from [http://docs.opencv.org/2.4/modules/calib3d/doc/camera\\_calibration\\_and\\_3d\\_reconstruction.html](http://docs.opencv.org/2.4/modules/calib3d/doc/camera_calibration_and_3d_reconstruction.html)
- Pierrot Deseilligny, M., & Clery, I. (2012). Apero, an Open Source Bundle Adjustment Software for Automatic Calibration and Orientation of Set of Images. *Isprs*, XXXV/III-5/(snavelly), 269–276. <http://doi.org/10.5194/isprsarchives-XXXVIII-5-W16-269-2011>
- Pix4D. (2016). Software for professional drone-based mapping. Retrieved February 3, 2016, from <https://www.pix4d.com/>
- Remondino, F., Barazzetti, L., Nex, F., Scaioni, M., & Sarazzi, D. (2011). UAV photogrammetry for mapping and 3D modeling – current status and future perspectives. *International Archives of the Photogrammetry, Remote Sensing and Spatial Information Sciences*, XXXV/III(September), 14–16. <http://doi.org/10.5194/isprsarchives-XXXVIII-1-C22-25-2011>
- Rosnell, T., & Honkavaara, E. (2012). Point cloud generation from aerial image data acquired by a quadcopter type micro unmanned aerial vehicle and a digital still camera. *Sensors*, 12(1), 453–480. <http://doi.org/10.3390/s120100453>
- Rublee, E., Rabaud, V., Konolige, K., & Bradski, G. (2011). ORB: An efficient alternative to SIFT or SURF. *Proceedings of the IEEE International Conference on Computer Vision*, 2564–2571. <http://doi.org/10.1109/ICCV.2011.6126544>
- Sauerbier, M., Siegrist, E., Eisenbeiss, H., & Demir, N. (2012). the Practical Application of Uav-Based Photogrammetry Under Economic Aspects. *ISPRS - International Archives of the Photogrammetry, Remote Sensing and Spatial Information Sciences*, XXXVIII-1/(September), 45–50. <http://doi.org/10.5194/isprsarchives-XXXVIII-1-C22-45-2011>
- Schenk, T. (2005). Introduction to Photogrammetry. *Department of Civil and Environmental Engineering and Geodetic Science, The Ohio State University*, 79–95. Retrieved from [http://gscphoto.ceegs.ohio-state.edu/courses/GeodSci410/docs/GS410\\_02.pdf](http://gscphoto.ceegs.ohio-state.edu/courses/GeodSci410/docs/GS410_02.pdf)
- Secret Labs AB. (2015). Python Imaging Library. Retrieved January 10, 2015, from <https://pypi.python.org/pypi/PIL>
- Shapiro, L., & Stockman, G. (2001). *Computer Vision*. October (Vol. 2004). <http://doi.org/10.1525/jer.2008.3.1.toc>
- Statistical Consultants Ltd. (2016). List of Free GIS Software. Retrieved February 1, 2016, from <http://lists.com/en/lists/e488pe.html>
- TERRISGPS. (2015). Using UAV GPS. Retrieved July 22, 2015, from <http://www.terrisgps.com/how-is-gps-used-in-uav/>
- The Institute For Mapping Technology. (2010). GIS Mapping Software. Retrieved February 1, 2016, from <http://learninggis.com/learn-about-gis/gis-mapping-software>
- Toutin, T., & Chénier, R. (2004). GCP requirement for high-resolution satellite mapping. *XXth ISPRS*

- Congress*, 12–23. Retrieved from <http://www.cartesia.org/geodoc/isprs2004/comm3/papers/385.pdf>
- Turner, D., Lucieer, A., & Watson, C. (2012). An automated technique for generating georectified mosaics from ultra-high resolution Unmanned Aerial Vehicle (UAV) imagery, based on Structure from Motion (SfM) point clouds. *Remote Sensing*, 4(5), 1392–1410. <http://doi.org/10.3390/rs4051392>
- Vedaldi, A. (2007). Scale Invariant Feature Transform(SIFT). Retrieved November 10, 2015, from <http://www.vlfeat.org/api/sift.html>
- Vedaldi, A., & Fulkerson, B. (2010). Vlfeat. *Proceedings of the International Conference on Multimedia - MM '10*, 3(1), 1469. <http://doi.org/10.1145/1873951.1874249>
- Visionmap. (2015). A3 Edge Digital Mapping Camera. Retrieved August 18, 2015, from [http://www.visionmap.com/en/products/A3-overview/A3\\_edge](http://www.visionmap.com/en/products/A3-overview/A3_edge)
- Wallace, L., Lucieer, A., Watson, C., & Turner, D. (2012). Development of a UAV-LiDAR system with application to forest inventory. *Remote Sensing*, 4(6), 1519–1543. <http://doi.org/10.3390/rs4061519>
- Wang, C., Stefanidis, A., Croitoru, A., & Agouris, P. (2008). Map Registration of Image Sequences Using Linear Features. *Photogrammetric Engineering & Remote Sensing*, 74(1), 25–38. <http://doi.org/10.14358/PERS.74.1.25>
- Wei, Y.-M., Kang, L., Yang, B., & Wu, L.-D. (2013). Applications of structure from motion: a survey \*. *J Zhejiang Univ-Sci C (Comput & Electron) Journal of Zhejiang University-SCIENCE C (Computers & Electronics)*, 14(7), 486–494. <http://doi.org/10.1631/jzus.CIDE1302>
- Xu, Z., Wu, L., Shen, Y., Li, F., Wang, Q., & Wang, R. (2014). Tridimensional Reconstruction Applied to Cultural Heritage with the Use of Camera-Equipped UAV and Terrestrial Laser Scanner, 10413–10434. <http://doi.org/10.3390/rs61110413>
- Yahyanejad, S., Wischounig-Struel, D., Quaritsch, M., & Rinner, B. (2010). Incremental mosaicking of images from autonomous, small-scale UAVs. *Proceedings - IEEE International Conference on Advanced Video and Signal Based Surveillance, AVSS 2010*, 329–336. <http://doi.org/10.1109/AVSS.2010.14>
- Zarco-Tejada, P. J., Diaz-Varela, R., Angileri, V., & Loudjani, P. (2014). Tree height quantification using very high resolution imagery acquired from an unmanned aerial vehicle (UAV) and automatic 3D photo-reconstruction methods. *European Journal of Agronomy*, 55, 89–99. <http://doi.org/10.1016/j.eja.2014.01.004>
- Zhang, Z. (1998). Determining the Epipolar Geometry and its Uncertainty: A Review. *International Journal of Computer Vision*, 27(2), 161–195. <http://doi.org/10.1023/a:1007941100561>

APPENDICES

Appendix 1: List of cameras

	A	B	C	D	E	F	G	H
1	P1000103_1400494888594	384311.6	5708790	258.3858				
2	P1000104_1400494888594	384323.1	5708782	257.6265				
3	P1000105_1400494888594	384335	5708774	257.0251				
4	P1000106_1400494888594	384347.6	5708766	256.7962				
5	P1000107_1400494888594	384359.9	5708757	256.9051				
6	P1000108_1400494888594	384372.3	5708749	256.8854				
7	P1000109_1400494888594	384384.4	5708740	256.983				
8	P1000110_1400494888594	384396.3	5708732	257.1115				
9	P1000111_1400494888594	384408.3	5708725	256.9434				
10	P1000112_1400494888594	384420.5	5708717	257.2053				
11	P1000113_1400494888594	384432.9	5708709	257.3163				
12	P1000114_1400494888594	384444.5	5708702	258.2887				
13	P1000115_1400494888594	384456.1	5708695	258.3276				
14	P1000116_1400494888594	384468.1	5708688	258.1164				
15	P1000117_1400494888594	384480	5708681	257.5677				
16	P1000118_1400494888594	384495.9	5708671	257.2506				
17	P1000119_1400494888594	384507.9	5708664	257.1514				
18	P1000120_1400494888594	384519.7	5708656	257.428				
19	P1000121_1400494888594	384531.3	5708648	257.5				
20	P1000122_1400494888594	384543.3	5708639	257.0155				
21	P1000123_1400494888594	384554.9	5708631	257.1019				
22	P1000124_1400494888594	384570.7	5708620	258.0925				
23	P1000125_1400494888594	384578.4	5708615	258.2725				
24	P1000126_1400494888594	384590.1	5708607	259.3225				
25	P1000127_1400494888594	384601.9	5708600	259.4772				
26	P1000128_1400494888594	384613.8	5708593	258.8826				
27	P1000129_1400494888594	384625.9	5708585	257.9406				
28	P1000130_1400494888594	384637.9	5708577	257.2007				
29	P1000191_1400494888594	384335	5708820	256.7102				
30	P1000192_1400494888594	384347.1	5708812	257.0421				
31	P1000193_1400494888594	384359.5	5708804	257.1404				
32	P1000194_1400494888594	384371.6	5708797	256.9149				
33	P1000195_1400494888594	384383.8	5708789	256.7296				
34	P1000196_1400494888594	384396.2	5708781	256.1713				
35	P1000197_1400494888594	384408.3	5708773	256.647				
36	P1000198_1400494888594	384420.5	5708766	256.2306				
37	P1000199_1400494888594	384432.9	5708758	256.8004				
38	P1000200_1400494888594	384445.1	5708750	256.9127				
39	P1000201_1400494888594	384457.4	5708743	256.92				
40	P1000202_1400494888594	384469.3	5708735	256.9046				
41	P1000203_1400494888594	384481.6	5708727	256.9052				
42	P1000204_1400494888594	384494.2	5708719	257.0824				
43	P1000205_1400494888594	384506.8	5708711	257.5645				
44	P1000206_1400494888594	384519	5708704	258.167				
45	P1000207_1400494888594	384531.7	5708696	257.386				
46	P1000208_1400494888594	384544.1	5708688	257.135				
47	P1000209_1400494888594	384556.7	5708680	257.2977				
48	P1000210_1400494888594	384569.3	5708672	257.5356				
49	P1000211_1400494888594	384582.1	5708664	257.3835				
50	P1000212_1400494888594	384595.2	5708656	256.7553				

Appendix 2: List of control points

	A	B	C	D	E	F	G	H
1	GCP100	384665.9	5708693	168.95				
2	GCP104	384714.6	5708738	169.032				
3	GCP11	384551.3	5708780	172.793				
4	GCP111	384537.6	5708773	170.55				
5	GCP116	384544.4	5708698	169.41				
6	GCP117	384539.5	5708688	169.41				
7	GCP124	384537.3	5708696	168.907				
8	GCP127	384539.7	5708695	168.696				
9	GCP128	384627.3	5708637	168.751				
10	GCP138	384597.8	5708589	170.608				
11	GCP14	384547.3	5708742	169.932				
12	GCP145	384334.9	5708786	169.367				
13	GCP149	384543.1	5708697	169.26				
14	GCP15	384547.2	5708742	169.953				
15	GCP150	384664.4	5708789	171.977				
16	GCP152	384538.8	5708688	169.38				
17	GCP155	384538.6	5708684	169.318				
18	GCP16	384545.6	5708733	169.955				
19	GCP162	384447.2	5708879	170.446				
20	GCP18	384543.6	5708820	171.509				
21	GCP19	384448.2	5708906	171.295				
22	GCP2	384438.5	5708887	170.812				
23	GCP21	384547.4	5708770	170.669				
24	GCP22	384479	5708855	170.927				
25	GCP23	384369.2	5708784	169.046				
26	GCP26	384535	5708825	171.637				
27	GCP29	384537.1	5708774	170.792				
28	GCP3	384560.3	5708738	170.481				
29	GCP32	384531.2	5708823	171.055				
30	GCP34	384550.5	5708783	172.292				
31	GCP35	384541.1	5708695	169.18				
32	GCP38	384548.7	5708774	170.723				
33	GCP4	384537.3	5708775	170.821				
34	GCP44	384550.8	5708646	169.075				
35	GCP45	384550.8	5708646	169.066				
36	GCP46	384567.5	5708628	170.54				
37	GCP5	384546.9	5708825	172.324				
38	GCP50	384606.4	5708579	168.973				
39	GCP51	384619.7	5708610	168.846				
40	GCP52	384622.8	5708604	169.039				
41	GCP53	384550.5	5708777	172.125				
42	GCP54	384447	5708878	170.49				
43	GCP55	384485.8	5708849	170.826				
44	GCP57	384627.2	5708637	168.751				
45	GCP59	384465.5	5708875	171.026				
46	GCP62	384447.3	5708879	170.515				
47	GCP63	384486.6	5708850	170.909				
48	GCP69	384617	5708606	168.878				
49	GCP7	384545.8	5708825	172.128				
50	GCP70	384617.6	5708602	168.803				

Appendix 3: List of control points and corresponding UAV image pixel coordinates

	A	B	C	D	E	F
1	P1000604_1400494888594.JPG	GCP100	3118.421	692.105		
2	P1000400_1400494888594.JPG	GCP100	2113.158	876.316		
3	P1000584_1400494888594.JPG	GCP104	2550	1944.737		
4	P1000583_1400494888594.JPG	GCP104	1765.789	1907.895		
5	P1000295_1400494888594.JPG	GCP111	823.684	2960.526		
6	P1000390_1400494888594.JPG	GCP111	2028.947	1113.158		
7	P1000612_1400494888594.JPG	GCP111	1965.789	855.263		
8	P1000295_1400494888594.JPG	GCP111	1328.947	2413.158		
9	P1000207_1400494888594.JPG	GCP116	1407.895	1534.211		
10	P1000211_1400494888594.JPG	GCP116	4207.895	1971.053		
11	P1000206_1400494888594.JPG	GCP117	423.684	3123.684		
12	P1000120_1400494888594.JPG	GCP117	1818.421	2939.474		
13	P1000520_1400494888594.JPG	GCP124	981.579	1960.526		
14	P1000207_1400494888594.JPG	GCP124	1671.053	1307.895		
15	P1000119_1400494888594.JPG	GCP124	1476.316	3160.526		
16	P1000209_1400494888594.JPG	GCP124	3123.684	1628.947		
17	P1000521_1400494888594.JPG	GCP127	1897.368	1613.158		
18	P1000208_1400494888594.JPG	GCP127	2365.789	1465.789		
19	P1000119_1400494888594.JPG	GCP127	1376.316	3171.053		
20	P1000216_1400494888594.JPG	GCP128	2739.474	1707.895		
21	P1000217_1400494888594.JPG	GCP128	3381.579	1581.579		
22	P1000328_1400494888594.JPG	GCP138	1713.158	713.158		
23	P1000327_1400494888594.JPG	GCP138	1197.368	865.789		
24	P1000296_1400494888594.JPG	GCP14	1139.474	1397.368		
25	P1000295_1400494888594.JPG	GCP14	313.158	1144.737		
26	P1000352_1400494888594.JPG	GCP145	534.211	3039.474		
27	P1000445_1400494888594.JPG	GCP145	1939.474	1102.632		
28	P1000209_1400494888594.JPG	GCP149	2902.632	1802.632		
29	P1000208_1400494888594.JPG	GCP149	2234.211	1607.895		
30	P1000207_1400494888594.JPG	GCP149	1444.737	1481.579		
31	P1000296_1400494888594.JPG	GCP15	1139.474	1386.842		
32	P1000298_1400494888594.JPG	GCP15	2650	1860.526		
33	P1000299_1400494888594.JPG	GCP15	3192.105	2081.579		
34	P1000612_1400494888594.JPG	GCP15	3118.421	1918.421		
35	P1000610_1400494888594.JPG	GCP15	1576.316	1728.947		
36	P1000300_1400494888594.JPG	GCP15	3750	2071.053		
37	P1000295_1400494888594.JPG	GCP15	307.895	1134.211		
38	P1000664_1400494888594.JPG	GCP150	1076.316	1539.474		
39	P1000577_1400494888594.JPG	GCP150	697.368	2313.158		
40	P1000207_1400494888594.JPG	GCP152	1450	955.263		
41	P1000211_1400494888594.JPG	GCP152	4276.316	1423.684		
42	P1000431_1400494888594.JPG	GCP152	3339.474	118.421		
43	P1000118_1400494888594.JPG	GCP155	571.053	2771.053		
44	P1000120_1400494888594.JPG	GCP155	1776.316	2760.526		
45	P1000210_1400494888594.JPG	GCP155	3560.526	1060.526		
46	P1000211_1400494888594.JPG	GCP155	4218.421	1244.737		
47	P1000431_1400494888594.JPG	GCP155	3428.947	260.526		
48	P1000430_1400494888594.JPG	GCP155	2771.053	155.263		
49	P1000296_1400494888594.JPG	GCP16	1034.211	928.947		
50	P1000300_1400494888594.JPG	GCP16	3686.842	1644.737		

**Appendix 4:** Pix4d Mapper report on residual at CPs when manually selected control points were used

0 out of 45 check pointss have been labeled as inaccurate.

Check Point Name	Accuracy XY/Z [m]	Error X[m]	Error Y [m]	Error Z [m]	Projection Error [pixel]	Verified/Marked
101	0.0200/0.0200	0.0285	-0.0051	0.0641	0.4820	25 / 25
102	0.0200/0.0200	0.0389	-0.0132	-0.1428	0.5432	37 / 37
103	0.0200/0.0200	0.0240	-0.0271	-0.2426	0.6792	43 / 43
104	0.0200/0.0200	0.0232	-0.0490	-0.2486	0.4759	48 / 48
105	0.0200/0.0200	0.0084	-0.0554	-0.1128	0.4855	19 / 19

106	0.0200/0.0200	-0.0084	-0.0651	-0.0314	0.5525	45 / 45
107	0.0200/0.0200	-0.0219	-0.0198	0.0194	0.5402	46 / 47
108	0.0200/0.0200	-0.0134	0.0102	0.3388	0.6488	34 / 34
109	0.0200/0.0200	-0.0234	0.0377	0.8993	0.4938	32 / 32
110	0.0200/0.0200	0.0282	-0.0132	-0.1429	0.5020	40 / 40
300	0.0200/0.0200	0.0051	-0.0243	-0.1135	0.5020	45 / 45
301	0.0200/0.0200	0.0105	-0.0255	-0.1517	0.6056	51 / 51
302	0.0200/0.0200	0.0007	-0.0294	-0.0638	0.6685	51 / 51
303	0.0200/0.0200	0.0072	-0.0019	0.0015	0.5927	49 / 49
304	0.0200/0.0200	0.0132	0.0067	0.0993	0.5941	47 / 47
305	0.0200/0.0200	0.0081	0.0159	0.3581	0.6517	45 / 45
306	0.0200/0.0200	0.0107	-0.0005	0.1133	0.5473	40 / 40
307	0.0200/0.0200	-0.0718	0.0093	0.7993	0.4647	42 / 42
308	0.0200/0.0200	-0.0377	0.0445	1.0183	0.4141	26 / 26
309	0.0200/0.0200	-0.0383	0.0438	1.0345	0.4714	26 / 26
310	0.0200/0.0200	-0.0003	0.0584	1.4151	0.5240	17 / 17
311	0.0200/0.0200	-0.0572	-0.0263	0.3195	0.4037	46 / 46
312	0.0200/0.0200	-0.0467	-0.0418	0.2490	0.5871	49 / 49
313	0.0200/0.0200	-0.0562	-0.0115	0.4508	0.5385	45 / 45
314	0.0200/0.0200	-0.0244	-0.0191	0.0429	0.5037	41 / 41
315	0.0200/0.0200	-0.0191	-0.0415	0.0044	0.6407	38 / 38
316	0.0200/0.0200	-0.0072	-0.0511	-0.0701	0.5261	49 / 49
317	0.0200/0.0200	-0.0175	-0.0359	-0.0448	0.4692	51 / 51
318	0.0200/0.0200	-0.0100	-0.0443	-0.1232	0.5628	41 / 41
319	0.0200/0.0200	-0.0105	-0.0469	-0.1195	0.4344	41 / 41
400	0.0200/0.0200	-0.0053	-0.0335	-0.1374	0.6684	45 / 45
401	0.0200/0.0200	-0.0014	-0.0606	-0.1316	0.5579	49 / 49
402	0.0200/0.0200	0.0059	-0.0757	-0.0450	0.5689	30 / 30
412	0.0200/0.0200	0.0154	0.0356	0.6512	0.6295	35 / 35
413	0.0200/0.0200	-0.0005	0.0096	0.6968	0.5530	21 / 21
414	0.0200/0.0200	0.0185	0.0227	0.3474	0.4470	29 / 29
415	0.0200/0.0200	0.0219	0.0049	-0.0113	0.5037	34 / 34
416	0.0200/0.0200	0.0069	-0.0343	-0.2302	0.6355	48 / 48
417	0.0200/0.0200	0.0190	-0.0248	-0.2538	0.5125	48 / 48
418	0.0200/0.0200	0.0223	-0.0576	-0.1691	0.5920	45 / 45
419	0.0200/0.0200	0.0194	-0.0602	-0.0300	0.4432	36 / 36
420	0.0200/0.0200	0.0233	-0.0685	0.1070	0.5051	31 / 31
421	0.0200/0.0200	0.0200	-0.0693	-0.0133	0.4697	30 / 30
422	0.0200/0.0200	0.0140	-0.0769	-0.0165	0.4041	37 / 37
423	0.0200/0.0200	0.0077	-0.0792	-0.0100	0.4777	40 / 40
<b>Mean [m]</b>		-0.001556	-0.021976	0.141644		
<b>Sigma [m]</b>		0.024857	0.035385	0.387947		
<b>RMS Error [m]</b>		0.024905	0.041654	0.412996		

**Appendix 5:** Pix4d Mapper report on residuals at CPs when automatically selected control points were used along with DSM

0 out of 38 check pointss have been labeled as inaccurate.

Check Point Name	Accuracy XY/Z [m]	Error X[m]	Error Y [m]	Error Z [m]	Projection Error [pixel]	Verified/Marked
101	0.0200/0.0200	-0.0186	-0.0533	0.2391	0.4357	12 / 12
102	0.0200/0.0200	-0.0151	-0.0388	0.1219	0.6272	19 / 19
105	0.0200/0.0200	0.0205	-0.0152	-0.3876	0.5664	19 / 19
106	0.0200/0.0200	0.0245	-0.0249	-0.4699	0.4395	18 / 18
107	0.0200/0.0200	0.0290	-0.0170	-0.3678	0.3846	21 / 22
108	0.0200/0.0200	0.0635	-0.0475	-0.2518	0.5543	14 / 14
109	0.0200/0.0200	0.0317	-0.0383	-0.0617	0.5140	21 / 21
110	0.0200/0.0200	0.0054	-0.0361	-0.0963	0.5448	19 / 19
300	0.0200/0.0200	0.0042	-0.0077	-0.2168	0.5740	18 / 18
301	0.0200/0.0200	0.0013	-0.0094	-0.1937	0.4971	25 / 25
302	0.0200/0.0200	-0.0039	-0.0296	-0.1185	0.6840	24 / 24
303	0.0200/0.0200	0.0063	-0.0179	-0.0952	0.5661	25 / 25
304	0.0200/0.0200	0.0097	-0.0329	-0.0423	0.6662	25 / 25
305	0.0200/0.0200	0.0046	-0.0403	0.0594	0.8447	24 / 24
306	0.0200/0.0200	-0.0138	-0.0416	0.0936	0.6971	20 / 20
307	0.0200/0.0200	0.0932	-0.0407	-0.2680	0.4934	19 / 19
308	0.0200/0.0200	0.0398	-0.0383	-0.0691	0.4486	15 / 15
309	0.0200/0.0200	0.0406	-0.0378	-0.0872	0.5729	16 / 16
310	0.0200/0.0200	0.0702	-0.0520	0.0736	0.6203	17 / 17
311	0.0200/0.0200	0.0775	-0.0195	-0.4214	0.3652	22 / 22
312	0.0200/0.0200	0.0656	-0.0279	-0.4443	0.4507	21 / 21
313	0.0200/0.0200	0.0842	-0.0404	-0.3224	0.4480	19 / 19
314	0.0200/0.0200	0.0194	-0.0059	-0.3292	0.4818	18 / 18
315	0.0200/0.0200	0.0196	-0.0115	-0.3657	0.4092	15 / 15
316	0.0200/0.0200	0.0166	-0.0190	-0.3976	0.6422	24 / 24
317	0.0200/0.0200	0.0068	-0.0103	-0.3246	0.5636	25 / 25
318	0.0200/0.0200	-0.0068	-0.0243	-0.2632	0.5186	14 / 14
319	0.0200/0.0200	-0.0092	-0.0212	-0.2808	0.4675	15 / 15
400	0.0200/0.0200	-0.0130	-0.0092	-0.1857	0.5983	22 / 22
401	0.0200/0.0200	-0.0109	-0.0222	-0.2313	0.5955	22 / 22
402	0.0200/0.0200	0.0147	-0.0336	-0.3595	0.5530	15 / 15
412	0.0200/0.0200	0.0200	-0.0454	0.1266	0.6759	26 / 26
413	0.0200/0.0200	-0.0363	-0.0854	0.5201	0.8748	19 / 19
415	0.0200/0.0200	-0.0281	-0.0343	0.1818	0.6003	18 / 18
418	0.0200/0.0200	-0.0261	-0.0139	0.0426	0.6719	19 / 19
421	0.0200/0.0200	-0.0391	0.0017	-0.0544	0.5491	10 / 10
422	0.0200/0.0200	-0.0166	-0.0090	-0.1595	0.4491	15 / 15
423	0.0200/0.0200	-0.0245	-0.0192	-0.1370	0.5697	15 / 15
<b>Mean [m]</b>		0.013340	-0.028152	-0.145898		
<b>Sigma [m]</b>		0.033509	0.016847	0.216169		
<b>RMS Error [m]</b>		0.036067	0.032808	0.260797		

**Appendix 6:** Pix4d Mapper report on residuals at CPs when automatically selected control points were used along with DTM

0 out of 38 check pointss have been labeled as inaccurate.

Check Point Name	Accuracy XYZ [m]	Error X [m]	Error Y [m]	Error Z [m]	Projection Error [pixel]	Verified/Marked
101	0.0200/0.0200	-0.0151	-0.0619	0.3238	0.4437	12 / 12
102	0.0200/0.0200	-0.0020	-0.0370	0.2699	0.6179	19 / 19
105	0.0200/0.0200	0.1188	-0.0438	0.0418	0.5838	19 / 19
106	0.0200/0.0200	0.1238	-0.0772	-0.1146	0.4355	18 / 18
107	0.0200/0.0200	0.0689	-0.0461	-0.2596	0.3863	21 / 22
108	0.0200/0.0200	0.0845	-0.0650	-0.2787	0.5613	13 / 13
109	0.0200/0.0200	0.0490	-0.0634	-0.1152	0.5057	21 / 21
110	0.0200/0.0200	0.0301	-0.0395	0.0445	0.5310	18 / 19
300	0.0200/0.0200	0.0607	-0.0206	0.0581	0.5828	18 / 18
301	0.0200/0.0200	0.0539	-0.0181	0.0726	0.4682	25 / 25
302	0.0200/0.0200	0.0353	-0.0378	0.0699	0.6590	24 / 24
303	0.0200/0.0200	0.0367	-0.0255	0.0327	0.5438	25 / 25
304	0.0200/0.0200	0.0299	-0.0431	0.0289	0.6361	24 / 25
305	0.0200/0.0200	0.0185	-0.0566	0.0667	0.8604	23 / 24
306	0.0200/0.0200	0.0002	-0.0500	0.1672	0.7132	20 / 20
307	0.0200/0.0200	0.0998	-0.0562	-0.5107	0.4896	19 / 19
308	0.0200/0.0200	0.0586	-0.0621	-0.1330	0.4731	15 / 15
309	0.0200/0.0200	0.0599	-0.0619	-0.1520	0.6264	16 / 16
310	0.0200/0.0200	0.0887	-0.0904	0.0456	0.6919	17 / 17
311	0.0200/0.0200	0.1027	-0.0787	-0.6002	0.4417	22 / 22
312	0.0200/0.0200	0.1095	-0.0973	-0.5325	0.5324	21 / 21
313	0.0200/0.0200	0.0940	-0.0742	-0.5213	0.4828	19 / 19
314	0.0200/0.0200	0.0692	-0.0398	-0.1759	0.5063	18 / 18
315	0.0200/0.0200	0.0859	-0.0525	-0.1414	0.3692	15 / 15
316	0.0200/0.0200	0.0995	-0.0553	-0.0759	0.6301	24 / 24
317	0.0200/0.0200	0.0733	-0.0406	-0.0633	0.5518	25 / 25
318	0.0200/0.0200	0.0609	-0.0401	0.0567	0.5230	14 / 14
319	0.0200/0.0200	0.0677	-0.0377	0.0860	0.4970	15 / 15
400	0.0200/0.0200	0.0526	-0.0171	0.1601	0.5943	22 / 22
401	0.0200/0.0200	0.0818	-0.0280	0.2435	0.5371	21 / 22
402	0.0200/0.0200	0.1232	-0.0638	0.1191	0.5528	15 / 15
412	0.0200/0.0200	0.0269	-0.0738	0.1140	0.7076	26 / 26
413	0.0200/0.0200	-0.0417	-0.1227	0.5722	0.9220	19 / 19
415	0.0200/0.0200	-0.0200	-0.0387	0.2866	0.5899	18 / 18
418	0.0200/0.0200	0.0580	0.0099	0.5844	0.6651	19 / 19
421	0.0200/0.0200	0.0857	0.0255	0.7135	0.5509	10 / 10
422	0.0200/0.0200	0.1082	0.0039	0.5362	0.9154	15 / 15
423	0.0200/0.0200	0.0914	-0.0239	0.5224	1.0028	15 / 15
<b>Mean [m]</b>		0.061290	-0.047401	0.040579		
<b>Sigma [m]</b>		0.040645	0.028465	0.306141		
<b>RMS Error [m]</b>		0.073542	0.055291	0.308819		